

Vertical shear instabilities in rotating stellar radiation zones: effects of the full Coriolis acceleration and thermal diffusion

J. Park,¹* S. Mathis,²

¹*Centre of Fluid and Complex Systems, Coventry University, Coventry CV1 5FB, UK*

²*Université Paris-Saclay, Université Paris Cité, CEA, CNRS, AIM, Gif-sur-Yvette, F-91191, France*

Accepted XXX. Received YYY; in original form ZZZ

ABSTRACT

Rotation deeply impacts the structure and the evolution of stars. To build coherent 1D or multi-D stellar structure and evolution models, we must systematically evaluate the turbulent transport of momentum and matter induced by hydrodynamical instabilities of radial and latitudinal differential rotation in stably stratified thermally diffusive stellar radiation zones. In this work, we investigate vertical shear instabilities in these regions. The full Coriolis acceleration with the complete rotation vector at a general latitude is taken into account. We formulate the problem by considering a canonical shear flow with a hyperbolic-tangent profile. We perform linear stability analysis on this base flow using both numerical and asymptotic Wentzel-Kramers-Brillouin-Jeffreys (WKBJ) methods. Two types of instabilities are identified and explored: inflectional instability, which occurs in the presence of an inflection point in shear flow, and inertial instability due to an imbalance between the centrifugal acceleration and pressure gradient. Both instabilities are promoted as thermal diffusion becomes stronger or stratification becomes weaker. Effects of the full Coriolis acceleration are found to be more complex according to parametric investigations in wide ranges of colatitudes and rotation-to-shear and rotation-to-stratification ratios. Also, new prescriptions for the vertical eddy viscosity are derived to model the turbulent transport triggered by each instability. We foresee that the inflectional instability will be responsible for turbulent transport in the equatorial region of strongly-stratified radiative zones in slowly rotating stars while the inertial instability triggers turbulence in the polar regions of weakly-stratified radiative zones in fast-rotating stars.

Key words: Hydrodynamics – turbulence – stars: rotation – stars: evolution

1 INTRODUCTION

The rotation of stars deeply modifies their evolution (e.g. Maeder 2009). In the case of rapidly-rotating stars, such as early-type stars (e.g. Royer et al. 2007) and young late-type stars (e.g. Gallet & Bouvier 2015), the centrifugal acceleration modifies their hydrostatic structure (e.g. Espinosa Lara & Rieutord 2013; Rieutord et al. 2016). Simultaneously, the Coriolis acceleration and buoyancy are governing the properties of large-scale flows (e.g. Garaud 2002; Rieutord 2006), waves (e.g. Dintrans & Rieutord 2000; Mathis 2009; Mirouh et al. 2016), hydrodynamical instabilities (e.g. Zahn 1983, 1992; Mathis et al. 2018), and magneto-hydrodynamical processes (e.g. Spruit 1999; Fuller et al. 2019; Jouve et al. 2020) that develop in their radiative regions. These regions are the seat of a strong transport of angular momentum occurring in all stars of all masses as revealed by space-based asteroseismology (e.g. Mosser et al. 2012; Deheuvels et al. 2014; Van Reeth et al. 2016) and of a mild mixing that modify the stellar structure and chemical stratification with multiple consequences from the life time of stars to their interactions with their surrounding planetary and galactic environments. After almost three decades of implementation of a large diversity of physical parametrisations of transport and mixing mechanisms in one-dimensional stellar evolution codes (e.g. Talon et al. 1997; Heger

et al. 2000; Meynet & Maeder 2000; Maeder & Meynet 2004; Heger et al. 2005; Talon & Charbonnel 2005; Decressin et al. 2009; Marques et al. 2013; Cantiello et al. 2014), stellar evolution modelling is now entering a new area with the development of a new generation of bi-dimensional stellar structure and evolution models such as the numerical code ESTER (Espinosa Lara & Rieutord 2013; Rieutord et al. 2016; Mombarg et al. 2023, 2024). This code simulates in 2D the secular structural and chemical evolution of rotating stars and their large-scale internal zonal and meridional flows. Similarly to 1D stellar structure and evolution codes, it needs physical parametrisations of small spatial scale and short time scale processes such as waves, hydrodynamical instabilities and turbulence. To model the evolution of rotating stars, we need to take coherently the combined action of the buoyancy force and of the full Coriolis acceleration into account for any value of their ratio (from the order of 10^2 in the bulk of the radiative core of main-sequence solar-type stars to $\sim 5-10$ in the bulk of the radiative envelope in rapidly-rotating main-sequence early-type stars). Walking on the path previously done for 1D codes, among all the necessary progresses, a first step is to examine the properties of the hydrodynamical instabilities of the vertical and horizontal shear of the differential rotation. Recent efforts have been devoted to improving the modelling of the turbulent transport triggered by the instabilities of the horizontal differential rotation in stellar radiation zones with buoyancy, the Coriolis acceleration and heat diffusion being considered (e.g. Park et al. 2020, 2021).

* E-mail: junho.park@coventry.ac.uk

However, strong vertical differential rotation also develops because of stellar structure's adjustments or the braking of the stellar surface by stellar winds (e.g. Zahn 1992; Meynet & Maeder 2000; Decressin et al. 2009). Up to now, state-of-the-art prescriptions for the turbulent transport it can trigger ignore the action of the Coriolis acceleration (e.g. Zahn 1992; Maeder 1995; Maeder & Meynet 1996; Talon & Zahn 1997; Prat & Lignières 2014a; Kulenthirarajah & Garaud 2018) or examine it in a specific equatorial set up (Chang & Garaud 2021). Therefore, it becomes mandatory to study the hydrodynamical instabilities of vertical shear by taking into account the combination of buoyancy, the full Coriolis acceleration and strong heat diffusion at any latitude.

Instability of vertically-sheared flow has been a subject of interest in fundamental fluid dynamics to understand its development towards turbulence (Miles 1961; Klaassen & Peltier 1985; Caulfield 2021). Two famous examples of vertical shear instability in stratified flows are the Kelvin-Helmholtz Instability (KHI) and Holmboe instability (Helmholtz 1868; Kelvin 1871; Holmboe 1962). KHI was originally studied for piecewise profiles of streamwise velocity $U(z)$ and density $\rho(z)$ but the instability can also be found in flows with smooth profiles of vertical shear dU/dz and negative density gradient $d\rho/dz < 0$, the latter corresponding to the case of stable density stratification. The Richardson's criterion states a necessary condition for instability in terms of the local Richardson number $Ri(z)$ as

$$Ri(z) = \frac{g(-d\rho/dz)}{\rho(dU/dz)^2} \leq \frac{1}{4}, \quad (1)$$

where g is the gravity (see also, Drazin 2015). KHI is typically expected to be stabilized by strong stratification when $Ri > 1/4$. However, in the layer where density gradient is sharp, the Holmboe instability can appear and plays an important role in mixing of stratified shear flows (Ortiz et al. 2002; Eaves & Balmforth 2019).

Wang et al. (2014) investigated more extensively instabilities of vertical shear flows in stratified and rotating fluids in which the rotation axis is along the vertical. Depending on the rotation, stratification, shear flow profiles and other parameters such as wavelengths of perturbation, they identified centrifugal instability as well as KHI for such vertical shear flows. The centrifugal instability occurs when there is an imbalance between the pressure gradient and centrifugal force due to the rotation. The instability is also called the inertial instability in the Cartesian coordinates (Holton 2004) and is analogous to the Goldreich-Schubert-Fricke (GSF) instability in the limit of high thermal diffusivity (Goldreich & Schubert 1967; Fricke 1968) and symmetric instability (Zeitlin 2018). For certain profiles of base flow, Wang et al. (2014) also identified another type of instability called the ageostrophic instability that occurs due to interactions between the shear and an inertia-gravity wave, or between two inertia-gravity waves. They demonstrated that different instabilities appear depending on the Rossby number Ro , a non-dimensional number that scales as the inverse of rotation (e.g. Ro is small when the rotation is strong), and the profile of shear flow. Despite their detailed investigation, their results can not be directly applied to understand instabilities in stellar radiation zones as the study has been conducted with relevance in geophysical contexts where thermal or density diffusion is weak, while strong thermal diffusion occurs in the radiation zones.

In highly diffusive and stably stratified fluids, Lignières et al. (1999) investigated vertical shear instability occurring due to an inflection point of the shear flow, which we call hereafter the inflectional instability. They identified that there is a self-similarity in the high thermal-diffusivity limit (or in the limit of low Péclet number Pe that scales as the inverse of the thermal diffusivity) where the marginal stability curves fall onto a single curve $k_x RiPe \simeq 0.117$ where k_x

is the horizontal wavenumber in the streamwise (longitudinal) direction x . The information on these critical Ri or the normalized number $R = RiPe$ is essential when proposing eddy-viscosity models used in the modelling of angular momentum transport and chemical mixing along stellar evolution (Zahn 1992; Prat & Lignières 2014b). At the same time, such a turbulence modelling needs to take into account both stratification and rotation to properly describe anisotropic transport in the radial and latitudinal directions in stellar radiation zones (e.g. Zahn 1992; Mathis et al. 2018). Recent progress in direct numerical simulations allows us to further investigate quantitatively the properties of this transport (Prat & Lignières 2013, 2014b; Chang & Garaud 2021; Garaud 2021). However, these works do not take the Coriolis acceleration into account or only in the equatorial plane.

Therefore, while vertical shear instabilities in stably stratified and rotating fluids have been studied in the broad contexts of astrophysics as well as geophysics, there are relatively few studies on the instabilities when the rotation is not aligned with the local vertical axis as illustrated in Fig. 1. To explore vertical shear instabilities at a general colatitude $0^\circ \leq \theta \leq 180^\circ$, we need to consider the full Coriolis acceleration with both vertical (radial) and horizontal (latitudinal) rotation components. Zeitlin (2018) investigated how symmetric instability, an analogue to the inertial instability, can be modified by the inclusion of the full Coriolis acceleration. Studies by Barker et al. (2019, 2020) and Dymott et al. (2023) investigated thoroughly the GSF instability with a linear shear profile at the equator or at a general colatitude, or with arbitrary shear profiles comprised of both vertical (radial) and horizontal (latitudinal) differential rotation. Their numerical simulations revealed various non-linear properties of the GSF instability such as turbulence and angular momentum transport, layering and zonal jet formation in a preferred direction between the local angular momentum gradient and the vector perpendicular to the rotation axis. While these studies unveiled remarkable properties of the GSF and symmetric instabilities of vertical shears, a limitation lies in their linear shear profile, which does not possess an inflection point and thus does not exhibit inflectional instability.

It is noteworthy that the inflectional instability is essential in studying strong shear-induced mixing in stellar interior (Brüggen & Hillebrandt 2001) and shear flow such a hyperbolic-tangent type flow has been used to verify the Richardson's criterion, which is in turn crucial to deduce effective eddy-viscosities (e.g. Zahn 1992; Maeder 1995; Maeder & Meynet 1996; Talon & Zahn 1997; Mathis et al. 2018). Our recent work (Park et al. 2020, 2021) studied horizontal shear instabilities with the hyperbolic tangent flow in wide ranges of parameters to reveal how the strong thermal diffusion and full Coriolis acceleration modify the inflectional and inertial instabilities. It is revealed that the full Coriolis acceleration is crucial to model horizontal shear instabilities at a general latitude. Nonetheless, this non-traditional rotation effect is still not fully understood in the context of vertical shear flows in rotating radiation zones.

This situation motivates our current study on vertical shear instabilities in rotating stellar radiation zones (Fig. 1), in which fluids are stably stratified, with a focus on the effects of both the strong thermal diffusion and full Coriolis acceleration. In Sect. 2, we formulate equations for linear stability analysis of a hyperbolic-tangent vertical shear flow in stratified and thermally diffusive fluids under the influence of the full Coriolis acceleration. In Sect. 3, we present examples of numerical results on inflectional and inertial instabilities of vertical shear flows and study parametric dependence of these instabilities. In Sect. 4, we perform the WKBJ analysis and derive analytical and asymptotic expressions of the dispersion relation for the inertial instability in the limits of either vanishing or very high thermal diffusivity. In Sect. 5, we explain the link between the inertial

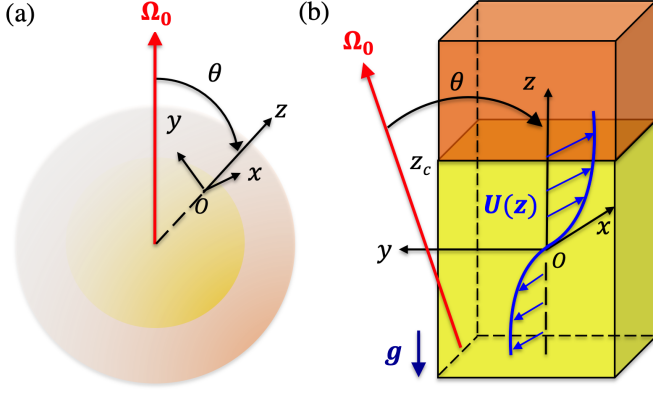


Figure 1. (a) Illustration of the radiation zone (yellow) and convective envelope (orange) of a low-mass star rotating with angular speed Ω_0 at the pole and the local coordinates (x, y, z) at a colatitude θ . (b) Vertical shear flow $U(z)$ on a local plane rotating with angular speed Ω_0 in the rotating stellar radiation zone. z_c is the transition altitude from the radiation zone to the convection zone.

instability and symmetric instability by demonstrating the mathematical equivalence between the two instabilities. In Sect. 6, we explore turbulent dissipation induced by vertical shear instabilities, derive a new prescription of eddy-viscosity and conduct parametric investigations for either inertial or inflectional instabilities. In Sect. 7, conclusion and discussion are presented.

2 PROBLEM FORMULATION

2.1 Governing equations and base state

We consider flow with shear along the vertical direction z at a general colatitude θ in the radiation zone of rotating stars (see e.g., the illustration of the interior of low-mass main-sequence stars in Fig. 1; the position of radiation and convection zones can be reversed for main-sequence early-type stars). The flow profile we consider here is relevant to shellular rotation where the angular rotation $\Omega(r)$ in stellar interior depends solely on the radial coordinate r of a star. Such a shellular approximation has been used to treat the angular momentum transport into one dimension (Zahn 1992). To investigate instabilities of vertical shear flow, we consider the Navier-Stokes equations in a rotating frame under the Boussinesq approximation, in which unstable and turbulent motions have characteristic spatial scales smaller than the density and pressure height scales, and the heat advection-diffusion equation in the Cartesian coordinates (x, y, z) (where x, y, z denote the local longitudinal, latitudinal and vertical coordinates, respectively) as follows:

$$\nabla \cdot \vec{u} = 0, \quad (2)$$

$$\frac{\partial \vec{u}}{\partial t} + (\vec{u} \cdot \nabla) \vec{u} + \vec{f} \times \vec{u} = -\frac{1}{\rho_0} \nabla p - \alpha_0 \Theta \vec{g} + \nu_0 \nabla^2 \vec{u}, \quad (3)$$

$$\frac{\partial \Theta}{\partial t} + \vec{u} \cdot \nabla \Theta = \kappa_0 \nabla^2 \Theta. \quad (4)$$

We introduce $\vec{u} = (u, v, w)$ as the velocity, p the pressure, $\Theta = T - T_0$ the temperature deviation from the reference temperature T_0 , $\vec{f} = (0, f_h, f_v)$ the Coriolis vector where $f_h = 2\Omega_0 \sin \theta$ and $f_v =$

$2\Omega_0 \cos \theta$ are its horizontal and vertical components, respectively, Ω_0 the reference angular rotation at the northern pole, $\vec{g} = (0, 0, -g)$ the gravity, ρ_0 the reference density, ν_0 the reference viscosity, κ_0 the reference thermal diffusivity, α_0 the thermal expansion coefficient, and $\nabla^2 = \partial^2/\partial x^2 + \partial^2/\partial y^2 + \partial^2/\partial z^2$ the Laplacian operator.

To perform linear stability analysis, we consider base velocity $\vec{U} = (U(z), 0, 0)$ with the vertically-sheared streamwise (longitudinal) velocity $U(z)$ in a canonical hyperbolic-tangent profile

$$U(z) = U_0 \tanh\left(\frac{z}{H_0}\right), \quad (5)$$

where U_0 and H_0 are the reference velocity and length scales, respectively. The base flow remains steady in time if the balance between $U(z)$, the base pressure $P(y, z)$ and the base temperature $\bar{T}(y, z)$ is maintained as follows:

$$\begin{aligned} f_v U &= -\frac{1}{\rho_0} \frac{\partial P}{\partial y}, \\ -f_h U &= -\frac{1}{\rho_0} \frac{\partial P}{\partial z} + \alpha_0 g \bar{T}. \end{aligned} \quad (6)$$

By eliminating the pressure in (6), we can obtain the following thermal-wind balance between the vertical shear $U(z)$ and the base temperature $\bar{T}(y, z)$

$$f_v \frac{\partial U}{\partial z} + \alpha_0 g \frac{\partial \bar{T}}{\partial y} = 0 \quad (7)$$

(see also, Wang et al. 2014). In addition, we assume that the base temperature is stably stratified in the vertical direction z with a linear profile with the constant temperature gradient $\mathcal{T}_\Theta > 0$. By considering this assumption and integrating the thermal-wind balance (7) in y , we find the base temperature as follows:

$$\bar{T}(y, z) = \mathcal{T}_\Theta z - \frac{f_v}{\alpha_0 g} \frac{\partial U}{\partial z} y. \quad (8)$$

2.2 Perturbation equations and linear stability analysis

In addition to the steady base state, we consider the velocity perturbation $\vec{u} = (\tilde{u}, \tilde{v}, \tilde{w}) = \vec{u} - \vec{U}$, the pressure perturbation $\tilde{p} = p - P$ and temperature perturbation $\tilde{T} = \Theta - \bar{T}$. Applying the perturbed state into the equations (2)-(4), we derive the following equations for the perturbations:

$$\frac{\partial \tilde{u}}{\partial x} + \frac{\partial \tilde{v}}{\partial y} + \frac{\partial \tilde{w}}{\partial z} = 0, \quad (9)$$

$$\frac{\partial \tilde{u}}{\partial t} + U \frac{\partial \tilde{u}}{\partial x} - f_v \tilde{v} + \left(\frac{\partial U}{\partial z} + f_h \right) \tilde{w} + \mathcal{N}_{\tilde{u}} = -\frac{1}{\rho_0} \frac{\partial \tilde{p}}{\partial x} + \nu_0 \nabla^2 \tilde{u}, \quad (10)$$

$$\frac{\partial \tilde{v}}{\partial t} + U \frac{\partial \tilde{v}}{\partial x} + f_v \tilde{u} + \mathcal{N}_{\tilde{v}} = -\frac{1}{\rho_0} \frac{\partial \tilde{p}}{\partial y} + \nu_0 \nabla^2 \tilde{v}, \quad (11)$$

$$\frac{\partial \tilde{w}}{\partial t} + U \frac{\partial \tilde{w}}{\partial x} - f_h \tilde{u} + \mathcal{N}_{\tilde{w}} = -\frac{1}{\rho_0} \frac{\partial \tilde{p}}{\partial z} + \alpha_0 g \tilde{T} + \nu_0 \nabla^2 \tilde{w}, \quad (12)$$

$$\frac{\partial \tilde{T}}{\partial t} + U \frac{\partial \tilde{T}}{\partial x} + \frac{\partial \tilde{T}}{\partial y} \tilde{v} + \frac{\partial \tilde{T}}{\partial z} \tilde{w} + \mathcal{N}_{\tilde{T}} = \kappa_0 \nabla^2 \tilde{T}, \quad (13)$$

where $\mathcal{N}_{\tilde{u}}$, $\mathcal{N}_{\tilde{v}}$, $\mathcal{N}_{\tilde{w}}$ and $\mathcal{N}_{\tilde{T}}$ are the nonlinear terms

$$\begin{aligned} \mathcal{N}_{\tilde{u}} &= \tilde{u} \frac{\partial \tilde{u}}{\partial x} + \tilde{v} \frac{\partial \tilde{u}}{\partial y} + \tilde{w} \frac{\partial \tilde{u}}{\partial z}, & \mathcal{N}_{\tilde{v}} &= \tilde{u} \frac{\partial \tilde{v}}{\partial x} + \tilde{v} \frac{\partial \tilde{v}}{\partial y} + \tilde{w} \frac{\partial \tilde{v}}{\partial z}, \\ \mathcal{N}_{\tilde{w}} &= \tilde{u} \frac{\partial \tilde{w}}{\partial x} + \tilde{v} \frac{\partial \tilde{w}}{\partial y} + \tilde{w} \frac{\partial \tilde{w}}{\partial z}, & \mathcal{N}_{\tilde{T}} &= \tilde{u} \frac{\partial \tilde{T}}{\partial x} + \tilde{v} \frac{\partial \tilde{T}}{\partial y} + \tilde{w} \frac{\partial \tilde{T}}{\partial z}. \end{aligned} \quad (14)$$

We note that the vertical temperature gradient

$$\frac{\partial \bar{T}}{\partial z} = \mathcal{T}_\Theta - \frac{f_v}{\alpha_0 g} \frac{\partial^2 U}{\partial z^2}, \quad (15)$$

is not homogeneous in the horizontal direction y if the second derivative $\partial^2 U / \partial z^2$ is not zero, which is the case for the hyperbolic-tangent profile. If we keep the second term on the right-hand side of Eq. (15), equations linearized from (9)-(13) cannot be expressed in a modal form due to the inhomogeneity in the y -direction. To avoid complexities of global stability analysis and simplify the problem, we assume that:

$$|y| \ll \left| \frac{\alpha_0 g \mathcal{T}_\Theta}{f_v} \right| / \max \left(\left| \frac{\partial^2 U}{\partial z^2} \right| \right), \quad (16)$$

which is called the wide jet approximation previously used for shear flows in geophysical contexts (Wang et al. 2014). The above assumption is valid if we limit our problem near $y = 0$ or when the vertical Coriolis parameter f_v is small (e.g., near the equator) while the vertical gradient \mathcal{T}_Θ is large. The approximation (16) can also be rewritten in a non-dimensional form as

$$\left| \frac{y}{H_0} \right| \ll \left| \frac{N^2 H_0}{f_v U_0} \right| = |Ri R_v|, \quad (17)$$

where $N = \sqrt{\alpha_0 g \mathcal{T}_\Theta}$ is the Brunt-Väisälä frequency, $Ri = N^2 / S_0^2$ is the Richardson number with $S_0 = U_0 / H_0$ the reference shear obtained from the vertical velocity gradient $\partial U / \partial z$ evaluated at $z = 0$, and $R_v = S_0 / f_v$ is the vertical Rossby number based on the vertical Coriolis parameter f_v . If we consider this wide jet approximation, we can neglect the second term on the right-hand side of Eq. (15) and the vertical temperature gradient $\partial \bar{T} / \partial z$ becomes constant as $\partial \bar{T} / \partial z \approx \mathcal{T}_\Theta$.

As we consider the approximation (16) and assume that the perturbation is infinitesimal (i.e., $N_{\hat{u}} = N_{\hat{v}} = N_{\hat{w}} = N_{\hat{T}} \approx 0$), we can perform linear stability analysis using the normal mode

$$\left(\tilde{u}, \tilde{p}, \tilde{T} \right) = \left(\hat{u}(z), \rho_0 \hat{p}(z), \mathcal{T}_\Theta \hat{T}(z) \right) \exp(i k_x x + i k_y y + \sigma t) + c.c., \quad (18)$$

where $c.c.$ denotes the complex conjugate, $i^2 = -1$, $\hat{u} = (\hat{u}, \hat{v}, \hat{w})$ is the velocity mode shape, \hat{p} and \hat{T} are the mode shapes for rescaled pressure and temperature perturbations, respectively, k_x is the horizontal wavenumber in the longitudinal direction x , k_y is the horizontal wavenumber in the latitudinal direction y , and $\sigma = \sigma_r + i\sigma_i$ is the complex growth rate where the real part σ_r denotes the temporal growth rate and the imaginary part σ_i denotes the temporal frequency. In terms of the wavenumber k_y , the approximation (16) can be equivalently expressed as

$$|k_y| \gg \max \left(\left| \frac{\partial^2 U}{\partial z^2} \right| \right) / \left(\left| \frac{\alpha_0 g \mathcal{T}_\Theta}{f_v} \right| \right), \quad (19)$$

which implies that the wavenumber k_y should be sufficiently large enough (i.e., the wavelength $\lambda_y = 2\pi/k_y$ should be small enough) to validate the wide jet approximation (see also, Wang et al. 2014). This also means that the latitudinal length scale of perturbations should be small compared to the length scale of the shear as the name ‘wide jet’ signifies. We can also define the cut-off minimum wavenumber $k_{y,\min}$ below which the wide jet approximation does not hold by rewriting (19) in terms of nondimensional parameters as

$$|k_{y,\min} H_0| \approx \frac{1}{|Ri R_v|}. \quad (20)$$

By applying the normal mode (18) to the perturbation equations

(9)-(13) with zero nonlinear terms, we obtain the following set of linear stability equations

$$i k_x \hat{u} + i k_y \hat{v} + \frac{d\hat{w}}{dz} = 0, \quad (21)$$

$$(\sigma + i k_x U) \hat{u} - f_v \hat{v} + (U' + f_h) \hat{w} = -i k_x \hat{p} + \nu_0 \hat{\nabla}^2 \hat{u}, \quad (22)$$

$$(\sigma + i k_x U) \hat{v} + f_v \hat{u} = -i k_y \hat{p} + \nu_0 \hat{\nabla}^2 \hat{v}, \quad (23)$$

$$(\sigma + i k_x U) \hat{w} - f_h \hat{u} = -\frac{d\hat{p}}{dz} + N^2 \hat{T} + \nu_0 \hat{\nabla}^2 \hat{w}, \quad (24)$$

$$(\sigma + i k_x U) \hat{T} - \frac{f_v U'}{N^2} \hat{v} + \hat{w} = \kappa_0 \hat{\nabla}^2 \hat{T}, \quad (25)$$

where prime ($'$) denotes the derivative with respect to z and $\hat{\nabla}^2 = d^2/dz^2 - k^2$ with $k^2 = k_x^2 + k_y^2$. In this study, we will use the following nondimensional parameters such as the Richardson number Ri , the Reynolds number Re , the Péclet number Pe , the Prandtl number Pr , the vertical and horizontal Rossby numbers R_v and R_h defined as

$$Re = \frac{U_0 H_0}{\nu_0}, \quad Pe = \frac{U_0 H_0}{\kappa_0}, \quad Pr = \frac{\nu_0}{\kappa_0} = \frac{Pe}{Re}, \quad (26)$$

$$Ri = \frac{N^2}{S_0^2} = \frac{\alpha_0 g \mathcal{T}_\Theta H_0^2}{U_0^2}, \quad R_v = \frac{S_0}{f_v}, \quad R_h = \frac{S_0}{f_h}.$$

For numerical computation, the linear stability equations (21)-(25) can be simplified into a matrix form with three variables \hat{u} , \hat{w} and \hat{T} as

$$\mathcal{A} \begin{pmatrix} \hat{u} \\ \hat{w} \\ \hat{T} \end{pmatrix} = \sigma \mathcal{B} \begin{pmatrix} \hat{u} \\ \hat{w} \\ \hat{T} \end{pmatrix}, \quad (27)$$

where \mathcal{A} and \mathcal{B} are the operator matrices in the form

$$\mathcal{A} = \begin{bmatrix} \mathcal{A}_{11} & \mathcal{A}_{12} & 0 \\ \mathcal{A}_{21} & \mathcal{A}_{22} & -N^2 k_y k^2 \\ -k_x f_v U' / (k_y N^2) & \mathcal{A}_{32} & \mathcal{A}_{33} \end{bmatrix},$$

$$\mathcal{B} = \begin{bmatrix} k^2 & -i k_x (d/dz) & 0 \\ 0 & k_y \hat{\nabla}^2 & 0 \\ 0 & 0 & 1 \end{bmatrix}, \quad (28)$$

where

$$\mathcal{A}_{11} = k^2 \left(-i k_x U + \nu_0 \hat{\nabla}^2 \right),$$

$$\mathcal{A}_{12} = \left(i k_y f_v - i k_x \nu_0 \hat{\nabla}^2 - k_x^2 U \right) \frac{d}{dz} - k_y^2 (U' + f_h),$$

$$\mathcal{A}_{21} = k^2 \left(i f_v \frac{d}{dz} - k_y f_h \right),$$

$$\mathcal{A}_{22} = i k_x k_y \left(U'' + f_h \frac{d}{dz} - U \hat{\nabla}^2 \right) + k_x f_v \frac{d^2}{dz^2} + k_y \nu_0 \hat{\nabla}^4,$$

$$\mathcal{A}_{32} = \frac{i f_v U'}{N^2 k_y} \frac{d}{dz} - 1,$$

$$\mathcal{A}_{33} = -i k_x U + \kappa_0 \hat{\nabla}^2.$$

For the case with $k_y = 0$, the eigenvalue problem (27) becomes singular in \mathcal{A}_{32} so we need to simplify differently the eigenvalue problem with different variables \hat{v} , \hat{w} , and \hat{T} as

$$\mathcal{C} \begin{pmatrix} \hat{v} \\ \hat{w} \\ \hat{T} \end{pmatrix} = \sigma \mathcal{D} \begin{pmatrix} \hat{v} \\ \hat{w} \\ \hat{T} \end{pmatrix}, \quad (30)$$

where \mathcal{C} and \mathcal{D} are the operator matrices

$$\mathcal{C} = \begin{bmatrix} C_{11} & C_{12} & 0 \\ C_{21} & C_{22} & -N^2 k_x^2 \\ f_v U' / N^2 & -1 & C_{33} \end{bmatrix}, \quad \mathcal{D} = \begin{bmatrix} 1 & 0 & 0 \\ 0 & \hat{\nabla}^2 & 0 \\ 0 & 0 & 1 \end{bmatrix}, \quad (31)$$

where

$$\begin{aligned} C_{11} &= -ik_x U + \nu_0 \hat{\nabla}^2, \\ C_{12} &= -\frac{if_v}{k_x} \frac{d}{dz}, \\ C_{21} &= -ik_x f_v \frac{d}{dz}, \\ C_{22} &= ik_x (U'' - U \hat{\nabla}^2) + \nu_0 \hat{\nabla}^4, \\ C_{33} &= -ik_x U + \kappa_0 \hat{\nabla}^2. \end{aligned} \quad (32)$$

For the case where the wavenumbers are zero as $k_x = k_y = 0$, we obtain $\hat{w} = 0$ from the continuity equation and the vanishing boundary condition as $|z| \rightarrow \infty$. Then we solve the eigenvalue problem for \hat{u} , \hat{v} , and \hat{T} as follows:

$$\begin{bmatrix} \nu_0 \hat{\nabla}^2 & f_v & 0 \\ -f_v & \nu_0 \hat{\nabla}^2 & 0 \\ 0 & f_v U' / N^2 & \kappa_0 \hat{\nabla}^2 \end{bmatrix} \begin{pmatrix} \hat{u} \\ \hat{v} \\ \hat{T} \end{pmatrix} = \sigma \begin{pmatrix} \hat{u} \\ \hat{v} \\ \hat{T} \end{pmatrix}. \quad (33)$$

To solve the eigenvalue problems (27), (30) or (33) numerically, we use in the z -direction the rational Chebyshev function that maps the spectral Chebyshev domain $z_{\text{cheb}} \in (-1, 1)$ onto the physical space $z \in (-\infty, \infty)$ by the mapping $z/Z_{\text{map}} = z_{\text{cheb}}/\sqrt{1 - z_{\text{cheb}}^2}$ where Z_{map} is the stretching factor in the mapping. In computing eigenmodes, we find both physical modes and spurious modes, the latter which are highly oscillatory. To distinguish physical modes from spurious modes, we apply a convergence criterion proposed by Fabre & Jacquín (2004) who studied the behaviour of solutions such that the physical modes should not be highly oscillatory and decays to zero as $|z| \rightarrow \infty$. In this case, the coefficients of the Chebyshev functions at high orders are sufficiently low. Also, in computation, we consider the number of collocation points in the z -direction between 100 and 200. We found that the number is sufficiently large to confirm the convergence of physical modes in our parameter space of interest. To impose vanishing boundary conditions as $|z| \rightarrow \infty$, we suppress the first and last rows of each element of the operator matrices (we refer to Antkowiak 2005; Park 2012, for more details).

2.3 Simplified equations in the inviscid limit $\nu_0 \rightarrow 0$

For the inviscid case ($\nu_0 = 0$), we can simplify the equations (21)–(25). By eliminating the pressure and considering the continuity equation, we obtain the following differential equations for \hat{w} and \hat{T} :

$$\begin{aligned} \frac{d^2 \hat{w}}{dz^2} &= \left(\frac{iN^2 k^2 s}{s^2 - f_v^2} \right) \hat{T} + \left[\frac{k_x U' f_v^2}{s(f_v^2 - s^2)} + \frac{ik_y f_v (U' + 2f_h)}{s^2 - f_v^2} \right] \frac{d\hat{w}}{dz} + \\ &\left[\frac{U''(k_x s + ik_y f_v)}{s^2 - f_v^2} + \frac{k_y (U' + f_h) (k_y f_h s + ik_x f_v U')}{s(f_v^2 - s^2)} + \frac{k^2 s^2}{s^2 - f_v^2} \right] \hat{w}, \end{aligned} \quad (34)$$

$$\begin{aligned} \frac{d^2 \hat{T}}{dz^2} &= \frac{1}{\kappa_0} \left[\frac{f_v U' (k_x f_v - is k_y)}{N^2 k^2 s} \frac{d\hat{w}}{dz} + \left(1 + \frac{ik_x k_y f_v U' (U' + f_h)}{N^2 k^2 s} \right) \hat{w} \right] \\ &+ \left(k^2 + \frac{is}{\kappa_0} \right) \hat{T}, \end{aligned}$$

where $s = -i\sigma + k_x U$ is the Doppler-shifted frequency (Park & Billant 2013a). The above equations can further be simplified into a single fourth-order ordinary differential equation (ODE) in terms of \hat{w} as follows:

$$\begin{aligned} (s^2 - f_v^2) \frac{d^2 \hat{w}}{dz^2} &+ 2f_v \left[\frac{k_x f_v U'}{s} - ik_y (U' + f_h) \right] \frac{d\hat{w}}{dz} \\ &+ \left[k^2 (N^2 - s^2) - U'' (k_x s + ik_y f_v) \right. \\ &\left. + k_y (U' + f_h) \left(\frac{2ik_x f_v U'}{s} + k_y f_h \right) \right] \hat{w} \\ &= \kappa_0 \left(W_4 \frac{d^4 \hat{w}}{dz^4} + W_3 \frac{d^3 \hat{w}}{dz^3} + W_2 \frac{d^2 \hat{w}}{dz^2} + W_1 \frac{d\hat{w}}{dz} + W_0 \hat{w} \right), \end{aligned} \quad (36)$$

where $\{W_i\}_{i \in [0,4]}$ are the operators as follows:

$$\begin{aligned} W_4 &= i \left(\frac{f_v^2}{s} - s \right), \quad W_3 = -ik_x U' \left(2 + \frac{3f_v^2}{s^2} \right) - \frac{k_y f_v}{s} (U' + 2f_h), \\ W_2 &= ik^2 s \left(2 - \frac{f_v^2}{s^2} \right) - \frac{3f_v U''}{s^2} (ik_x f_v + k_y s) - \frac{ik_y^2 f_h (U' + f_h)}{s} \\ &+ \frac{k_x f_v U'}{s^2} \left(5k_y f_h + 3k_y U' + \frac{6ik_x f_v U'}{s} \right), \\ W_1 &= k^2 \left[ik_x U' \left(2 + \frac{f_v^2}{s^2} \right) + \frac{k_y f_v (U' + 2f_h)}{s} \right] \\ &+ U'''' \left[ik_x \left(2 - \frac{f_v^2}{s^2} \right) - \frac{3k_y f_v}{s} \right] + \frac{2ik_x k_y^2 f_h U' (U' + f_h)}{s^2} \\ &+ U'' \left(\frac{6ik_x^2 f_v^2 U'}{s^3} + \frac{9k_x k_y f_v U'}{s^2} + \frac{4k_x k_y f_v f_h}{s^2} - \frac{2ik_y^2 f_h}{s} \right) \\ &- \frac{2k_x^2 f_v U'^2}{s^3} \left(4k_y f_h + 3k_y U' + \frac{3ik_x f_v U'}{s} \right), \\ W_0 &= k^2 \left[\frac{U'' k_y f_v}{s} - ik^2 s - (U' + f_h) \left(\frac{k_x k_y f_v U'}{s^2} - \frac{ik_y^2 f_h}{s} \right) \right] \\ &+ U'''' \left(ik_x - \frac{k_y f_v}{s} \right) + \frac{k_y U''''}{s^2} [4k_x f_v U' + f_h (k_x f_v - ik_y s)] \\ &+ \frac{k_x k_y U''}{s^2} \left(3ik_y f_h U' - \frac{6k_x f_v f_h U'}{s} + 3f_v U'' + ik_y f_h^2 \right. \\ &\left. - \frac{12k_x f_v U'^2}{s} \right) + \frac{2k_x^2 k_y U'^2 (U' + f_h)}{s^3} \left(\frac{3k_x f_v U'}{s} - ik_y f_h \right). \end{aligned} \quad (37)$$

If we also consider non-diffusive fluids (i.e., $\kappa_0 = 0$), the right-hand side of the ODE (36) is zero and the equation (36) becomes a second-order ODE.

3 NUMERICAL RESULTS ON VERTICAL SHEAR INSTABILITIES

In this section, we present exemplary numerical results from linear stability analysis to understand effects of stratification, thermal diffusion and rotation on vertical shear instabilities. The combined effects of the stratification and thermal diffusion on the inflectional instability were extensively studied by Lignières et al. (1999), thus

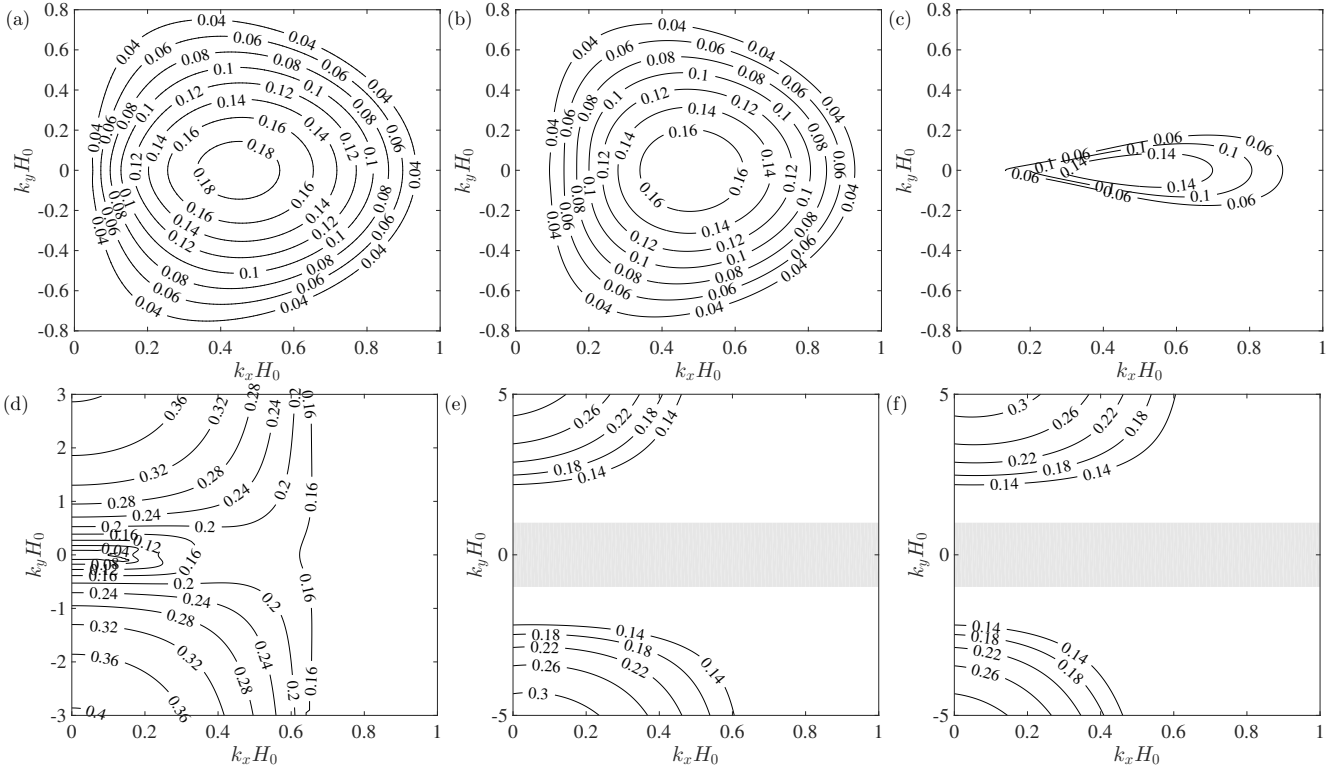


Figure 2. Contours of the growth rate σ_r/S_0 in the parameter space of wavenumbers (k_x, k_y) for a highly diffusive and inviscid fluid with $Pe = 0.01$ and $Re = \infty$ for (a) $(Ri, R_h, R_v) = (0.01, \infty, \infty)$ (a non-rotating case), (b) $(Ri, R_h, R_v) = (1, \infty, \infty)$ (a non-rotating case), (c) $(Ri, R_h, R_v) = (1, 1, \infty)$ (a rotating case at the equator $\theta = 90^\circ$ with $\Omega_0/S_0 = 0.5$), (d) $(Ri, R_h, R_v) = (1, -2, \infty)$ (a rotating case at the equator $\theta = 90^\circ$ with $\Omega_0/S_0 = -0.25$), (e) $(Ri, R_h, R_v) = (1, \infty, 1)$ (a rotating case either at the northern pole $\theta = 0^\circ$ with $\Omega_0/S_0 = 0.5$ or at the southern pole $\theta = 180^\circ$ with $\Omega_0/S_0 = -0.5$), and (f) $(Ri, R_h, R_v) = (1, \infty, -1)$ (a rotating case either at the northern pole $\theta = 0^\circ$ with $\Omega_0/S_0 = -0.5$ or at the southern pole $\theta = 180^\circ$ with $\Omega_0/S_0 = 0.5$). In panels e and f, the grey-shaded area denotes the range $|k_y H_0| \leq |Ri R_v|^{-1}$ of (20) where the wide-jet approximation is not valid.

we focus on the effects of rotation with the full Coriolis acceleration on vertical shear instabilities. Figure 2 shows representative examples of contours of the growth rate σ_r of the most unstable mode in the wavenumber space (k_x, k_y) for various sets of parameters (Ri, R_h, R_v) at $Pe = 0.01$ and $Re = \infty$, the case where the fluid is inviscid and highly diffusive. For all cases in Figure 2, the frequency σ_i of the most unstable mode is found to be zero. In panels a and b, we vary stratification by changing Ri for the non-rotating case $\Omega_0 = 0$ (i.e., $R_h = R_v = \infty$), in which only the inflectional instability exists. The growth-rate contours in panel a for $Ri = 0.01$ resemble those of the unstratified case at $Ri = 0$ in Delonche et al. (2007) and we find the maximum growth rate as $\sigma_{\max}/S_0 \approx 0.1894$ at $(k_x H_0, k_y H_0) \approx (0.45, 0)$. As the Richardson number increases to $Ri = 1$ (panel b), the inflectional instability is weakened and the maximum growth rate is reduced as $\sigma_{\max}/S_0 \approx 0.1767$ which is attained at $(k_x H_0, k_y H_0) \approx (0.47, 0)$. In panel c and d, we now consider rotating cases with $f_h \neq 0$ and $f_v = 0$ (i.e., $R_v = \infty$), the cases at the equator of a star with differential rotation in the radial direction (i.e., shellular rotation). Such a configuration with vertical (radial) shear and rotation perpendicular to the shear is equivalent to that with horizontal shear under the traditional f -plane approximation (Park et al. 2020). In light of this consideration, if $f_v = 0$, we expect the hyperbolic-tangent base flow (5) is inertially unstable if $-S_0 < f_h < 0$ (i.e., $R_v < -1$) according to the Rayleigh criterion in rotating fluids (Kloosterziel & van Heijst 1991; Park 2012; Park et al. 2020). We see in panel c that the cyclonic rotation case with $f_h > 0$ has no inertial instability, which occurs for large k_y , while the in-

flexional instability is suppressed significantly as we can see that the regime of instability shrinks in the wavenumber space (k_x, k_y) . We note, however, that this cyclonic case has the maximum growth rate $\sigma_{\max}/S_0 \approx 0.1767$ at $(k_x H_0, k_y H_0) \approx (0.47, 0)$, which is the same as the non-rotating case in panel b. This invariance of the growth rate for a two-dimensional inflectional instability (i.e., $k_y = 0$) is due to the fact that the fourth-order ODE (36) becomes invariant with f_h if we consider $k_y = f_v = 0$ as follows:

$$s \left\{ s \frac{d^2 \hat{w}}{dz^2} + \left[k_x^2 \left(\frac{N^2}{s} - s \right) - k_x U'' \right] \hat{w} \right\} + i \kappa_0 \left[s \frac{d^4 \hat{w}}{dz^4} + 2k_x U' \frac{d^3 \hat{w}}{dz^3} - 2k_x^2 s \frac{d^2 \hat{w}}{dz^2} - 2k_x \left(k_x^2 U' + U'''' \right) \frac{d \hat{w}}{dz} + k_x \left(k_x^3 s - U'''' \right) \hat{w} \right] = 0. \quad (38)$$

We see that the equation is no longer dependent on f_h .

For the anticyclonic case with $f_h/S_0 = -0.5$ (i.e., $R_v = -2$), the flow is inertially unstable and thus both the inertial and inflectional instabilities co-exist. From the growth rate contours in panel d, we found that the growth rate reaches its local maximum $\sigma/S_0 \approx 0.1767$ at $(k_x H_0, k_y H_0) \approx (0.47, 0)$ corresponding to the inflectional instability while the global maximum growth rate $\sigma_{\max}/S_0 \approx 0.5$ is attained as $|k_y| \rightarrow \infty$ at $k_x = 0$ due to the inertial instability. The growth rate contours in panel d are reminiscent of those for horizontal shear instabilities in rotating stellar radiation zones with the traditional f -plane approximation (Park et al. 2020). In panels e and f, we now consider rotating cases with $f_v \neq 0$ and $f_h = 0$ (i.e., $R_h = \infty$), which correspond to configurations at the poles where

the vertical shear varies along the direction of the Coriolis vector. The situation is analogous to horizontal shear cases at the equator when the full Coriolis acceleration is taken into account (Park et al. 2021). For vertical shear at the poles, the classical Rayleigh criterion based on the traditional f -plane approximation is no longer valid and thus we need to derive a new criterion for the inertial instability, which is presented in Sect. 4. In panels e and f where the vertical Rossby numbers are non-zero as $R_v = \pm 1$, we delimit the zones where the wide jet approximation is not valid for small $|k_y|$ as $|k_y H_0| < |k_{y,\min} H_0| = 1/|R_i R_v|$ according to (20). Unlike other cases in panels a–d, there is no inflectional instability in panels e and f in the parameter space of validity $|k_y| \geq |k_{y,\min}|$ and only the inertial instability is found for sufficiently large k_y . For the positive vertical Rossby number case $R_v = 1$, the growth rate tends to be larger in the lower half ($k_y < 0$) while the maximum growth rate $\sigma_{\max}/S_0 \approx 0.455$ is, however, attained in both limits: $k_y \rightarrow \pm\infty$ at $k_x = 0$. The growth rate at the negative vertical Rossby number $R_v = -1$ is larger in the upper half ($k_y > 0$) while the maximum growth rate $\sigma_{\max}/S_0 \approx 0.455$ is attained as $|k_y| \rightarrow \infty$ at $k_x = 0$. Growth-rate contours in panels e and f with $R_v = \pm 1$ are mirrored by the line $k_y = 0$ since the fourth-order ODE (36) is invariant with the substitution $(k_y, f_v) \rightarrow (-k_y, f_v)$ when $f_h = 0$.

3.1 Inflectional instability

Panels a and b in Fig. 3 show the eigenfunction $\hat{w}(z)$ and the corresponding perturbation $w(x, z) = \text{Re}[\hat{w}(z) \exp(ik_x x)]$ (where Re denotes the real part) for $Pe = 0.01$, $Re = \infty$, $Ri = 1$, $(R_h, R_v) = (-2, \infty)$ and $(k_x H_0, k_y H_0) = (0.47, 0)$. The perturbation at these wavenumbers corresponds to the inflectional instability mode that has a characteristic of being tilted against the base shear flow $U(z)$. The tilted feature is responsible for the growth via the Orr mechanism and is similarly observed for the inflectional instability in other types of shear flows including horizontal shear flows (Park et al. 2020, 2021).

The inflectional instability is present regardless of rotation. For a non-rotating case $\Omega_0 = 0$ or a rotating case at the equator $\theta = 90^\circ$ (i.e., $f_v = 0$ and $f_h \neq 0$), the growth rate of the inflectional instability is found to be maximal for two-dimensional modes at $k_y = 0$ and a non-zero k_x in the wavenumber range $0 < k_x H_0 < 1$ as shown by panels a–c of Fig. 2. In this case, it is found that three-dimensional inflectional instability modes with non-zero k_x and k_y have smaller growth rates than those of two-dimensional instability modes at $k_y = 0$. At $\Omega_0 = k_y = 0$, Fig. 4a shows examples of the inviscid growth rate of the inflectional instability versus k_x for different values of Pe and Ri . On the one hand, we see that the growth-rate curves descend as Ri increases at a fixed $Pe = 0.01$, which implies that stratification suppresses the inflectional instability. On the other hand, at a fixed $Ri = 1$, the growth-rate curves ascend as Pe decreases implying the promotion of the inflectional instability by the thermal diffusion. It is also noteworthy that the growth rates are quantitatively similar for the same $RiPe$ for low Pe (e.g. the case with $(Ri, Pe) = (1, 0.01)$ and the other with $(Ri, Pe) = (0.1, 0.1)$ where both have $RiPe = 0.01$). These self-similar results in the low-Péclet number limit are expected and well described by Lignières et al. (1999) for the non-rotating case. It is not shown here but, as expected, the viscosity with $\nu_0 > 0$ stabilizes the inflectional instability.

For rotating cases outside the equator (i.e. $\theta \neq 90^\circ$ and $f_v \neq 0$), the wide-jet approximation (20) needs to be taken into account. In this case, we found that three-dimensional modes with $k_y = k_{y,\min}$ and a non-zero k_x in the range $0 < k_x H_0 < 1$ have the maximum growth rate in the southern hemisphere $90^\circ < \theta < 180^\circ$ while the

modes at $k_y = -k_{y,\min}$ and for $0 < k_x H_0 < 1$ have the maximum growth rate in the northern hemisphere $0^\circ < \theta < 90^\circ$. We pick up the maximum of the growth rate σ_{\max} over the range $0 < k_x H_0 < 1$ at $|k_y| = |k_{y,\min}|$ and for a fixed rotation-to-stratification ratio Ω_0/N , Ri and Pe , and we display in panel b of Fig. 4 the maximum growth rate as a function of Ω_0/N for two cases: one at the equator $\theta = 90^\circ$ and the other in the southern hemisphere $\theta = 100^\circ$. At the equator, the inflectional instability is independent of the ratio Ω_0/N and thus its growth rate is invariant at a given Ri and Pe . The inflectional instability is promoted slightly as the thermal diffusion becomes stronger (i.e., as Pe decreases). In the southern hemisphere at $\theta = 100^\circ$, for weakly stratified cases with $Ri = 0.01$ at both $Pe = \infty$ and $Pe = 0.01$, the instability is strongly suppressed as the ratio Ω_0/N increases. At $Pe = 0.01$, the instability sustains for a high ratio of Ω_0/N as Ri increases although the growth rate at $\Omega_0 = 0$ is smaller for a larger Ri . As the latitude is further away from the equator, the inflectional instability tends to be suppressed faster as the ratio Ω_0/N increases. This is clearly shown in Fig. 4c by the contours of the maximum growth rate over the parameter space $(\theta, \Omega_0/N)$ at $Ri = 1$, $Pe = 0.01$ and now in a viscous case with $Pr = 10^{-6}$ (i.e., $Re = Pe/Pr = 10^4$). As Ω_0/N increases, the inflectional instability is suppressed as the co-latitude θ is away from the equator while the growth rate is invariant with the ratio Ω_0/N at the equator $\theta = 90^\circ$. The growth rate contours are symmetric with respect to the equator. This result implies that the inflectional instability is maximal near the equator and turbulent energy dissipation, momentum transport and matter mixing induced by the inflectional instability are therefore expected to be localised near the equator of fast-rotating stars and to vanish in polar regions. This latitudinal dependence is due to the action of the Coriolis acceleration. When its strength increases, gravito-inertial modes, which can become unstable because of the inflectional instability, become trapped around the equator (e.g. Lee & Saio 1997; Dintrans & Rieutord 2000). Therefore, it becomes mandatory to take into account the latitudinal dependences of hydrodynamical instabilities because of the Coriolis acceleration. More results on these turbulent processes are discussed in Sect. 6.2.

3.2 Inertial instability

Panels c and d in Fig. 3 display the eigenfunction $\hat{w}(z)$ and perturbation $w(x, z)$ at $(k_x H_0, k_z H_0) = (0.47, 5)$, the case that corresponds to the inertial instability mode. The eigenfunction has a wavelike structure around $|z| < 1$ while it is evanescent and decreases exponentially as $|z| \rightarrow \infty$. This mode corresponds to the first mode that has the fewest zero-crossings; i.e., 1 and 2 zero-crossings in the imaginary and real parts of the eigenfunction \hat{w} , respectively. There are also higher-order modes with more zero-crossings along z but we focus on the first mode with least zero-crossings since it is the most unstable mode. The existence of the inertial instability modes at the first and higher orders will also be discussed with quantization conditions derived by the WKB analysis in the next section.

Figure 5 shows examples of the growth rate of the inertial instability at $k_x = 0$, $Re = \infty$, $Pe = 0.01$, and $Ri = 1$ for various Ω_0 and θ . The anti-cyclonic rotation with $\Omega_0/S_0 = -0.25$ at the equator $\theta = 90^\circ$ (i.e., $f_h/S_0 = -0.5$ and $f_v = 0$, the case corresponding to the traditional f -plane approximation) drives the inertial instability. The growth rate of the inertial instability increases with k_y and asymptotes as $k_y \rightarrow \infty$. Such an asymptotic behavior is also observed for non-zero k_x cases (see e.g. black-dashed line for the case with $k_x H_0 = 0.47$) where the growth rate at $k_y = 0$ is above zero due to the inflectional instability. Nevertheless, the overall growth rate at $k_x H_0 = 0.47$ is smaller than the growth rate of the

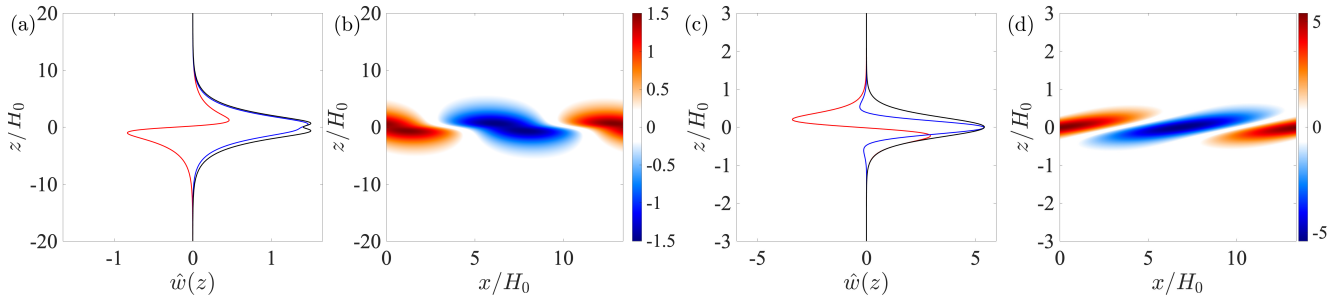


Figure 3. (a,c) Eigenfunction $\hat{w}(z)$ and (b,d) perturbation $w(x, z)$ for $Pe = 0.01$, $Re = \infty$, $Ri = 1$, $(R_h, R_v) = (-2, \infty)$ (i.e. $\theta = 90^\circ$ and $\Omega_0/S_0 = -0.25$) for (a,b) the inflectional-instability mode at $(k_x H_0, k_z H_0) = (0.47, 0)$ and (c,d) the inertial-instability mode at $(k_x H_0, k_z H_0) = (0.47, 5)$. In (a) and (c), blue, red, and black lines denote the real, imaginary, and absolute parts of the eigenfunction \hat{w} , respectively.

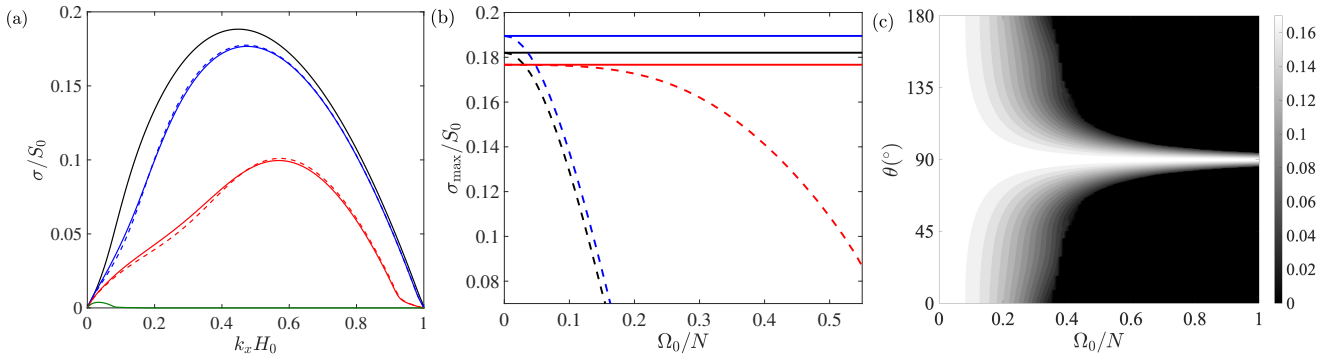


Figure 4. (a) Growth rate σ of the inflectional instability versus wavenumber k_x at $k_y = 0$, $\Omega_0 = 0$ and $Re = \infty$ for various sets of parameters (Pe, Ri) : (0.01,0.1) (black solid), (0.01,1) (blue solid), (0.01,10) (red solid), (0.1,0.1) (blue dashed), (0.1,1) (red dashed), and (1,1) (green solid). (b) Maximum inviscid growth rate σ_{\max} versus the ratio Ω_0/N at the equator (solid lines) and $\theta = 100^\circ$ (dashed lines) for $(Ri, Pe) = (0.01, \infty)$ (black), $(Ri, Pe) = (0.01, 0.01)$ (blue) and $(Ri, Pe) = (1, 0.01)$ (red). (c) Contours of the maximum growth rate σ_{\max}/S_0 in the parameter space $(\theta, \Omega_0/N)$ at $Ri = 1$, $Pe = 0.01$ and $Pr = 10^{-6}$.

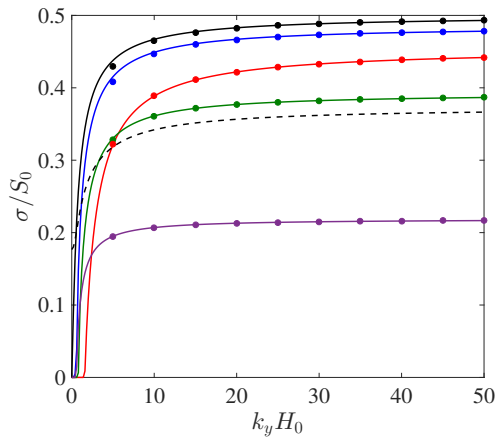


Figure 5. Growth rate σ of the first mode of the inertial instability versus wavenumber k_y for $k_x = 0$ (solid lines) and $k_x H_0 = 0.47$ (dashed line) at $Re = \infty$, $Pe = 0.01$, and $Ri = 1$ for various sets of parameters $(\Omega_0/S_0, \theta)$: $(-0.25, 90^\circ)$ (black), $(-0.25, 45^\circ)$ (blue), $(-0.5, 0^\circ)$ (red), $(-0.25, 0^\circ)$ (green), and $(0.25, 135^\circ)$ (purple). Filled circles denote predictions from the WKBJ asymptotic dispersion relation (80).

case with $k_x = 0$. We note that the asymptotic behavior of the inertial instability as $k_y \rightarrow \infty$ allows us to use the WKBJ approximation, as previously applied to many other studies on the inertial instability of shear flows and centrifugal instability of vortices in stably stratified-rotating fluids (Park & Billant 2013a; Park et al. 2020).

As the co-latitude θ decreases to zero (i.e., at the northern pole) while keeping the same rotation ratio $\Omega_0/S_0 = -0.25$, we see that the inertial instability is slightly suppressed. Such suppression also occurs as the co-latitude θ increases to $\theta = 180^\circ$ (i.e., at the southern pole) and it is found that the growth rates of at co-latitudes θ and $180^\circ - \theta$ are the same when the same rotation Ω_0 is applied in the low- Pe limit. We also see in Fig. 5 how the growth rate curves vary as the magnitude $|\Omega_0|$ or the sign of Ω_0 change.

From linear stability analysis in the inviscid limit $\nu_0 = 0$, the parametric dependence is numerically investigated for both the inflectional and inertial instabilities. In general, the inflectional instability has the maximum growth rate in the wavenumber range $0 < k_x H_0 < 1$ at $k_y = 0$ and tends to be suppressed by the stratification while strong thermal diffusion promotes the inflectional instability up to the level equivalent to the unstratified case. At the equator where $f_v = 0$, the three-dimensional inflectional instability with $k_y \neq 0$ is stabilised by the horizontal component f_h of the rotation vector while the maximum growth rate attained for two-dimensional perturbation with $k_y = 0$ is independent of f_h . The inflectional instability is suppressed as the co-latitude θ is off the equator and as the ratio Ω_0/N increases. For the inertial instability, it is clearly shown that its maximum growth rate is attained as $k_y \rightarrow \infty$ at $k_x = 0$. We identified that the maximum growth rate of the inertial instability is higher for certain parameter sets of Ω_0 , Pe and Ri than the maximum growth rate of the inflectional instability, which is $\sigma_{\max}/S_0 = 0.1807$ obtained for the unstratified case. However, understanding the dependence on the rotation Ω_0 , the co-latitude

θ , and other parameters is more difficult for the inertial instability from numerical investigations. In the following section, we will apply the WKBJ approximation and derive analytic expressions of the dispersion relation to understand more explicitly the parametric dependence of the inertial instability.

4 INERTIAL INSTABILITY AND WKBJ ANALYSIS

Thanks to the nature of the inertial instability that occurs for large k_y , we can perform an asymptotic analysis in the limit $k_y \rightarrow \infty$ using the WKBJ approximation to derive analytical expressions of the dispersion relation and understand explicitly how the inertial instability varies with different parameters. The WKBJ method is useful to approximate solutions of ordinary differential equations (ODEs) such as Eq. (36), which is obtained at $\nu_0 = 0$. The method is efficient to describe fast-oscillating wavelike solutions or evanescent solutions when a small parameter δ is considered. For the inertial instability, the parameter δ can be chosen by a proper scaling with large k_y based on observation of the eigenmode which oscillates faster as k_y increases. We can obtain the WKBJ solutions from (36) for two cases: a non-diffusive case with $\kappa_0 = 0$ and a highly-diffusive case as $\kappa_0 \rightarrow \infty$. We only consider for simplicity the zero streamwise wavenumber (i.e., $k_x = 0$) at which the growth rate of the inertial instability is maximal. In the next subsections, the WKBJ solutions for inertial instability modes, asymptotic dispersion relations, and parametric dependence will be discussed case by case.

4.1 WKBJ analysis for non-diffusive cases with $\kappa_0 = 0$

For the zero wavenumber $k_x = 0$ and adiabatic configuration where there is no viscous and thermal diffusion ($\nu_0 = \kappa_0 = 0$), the fourth-order ODE (36) can be simplified into the second-order ODE as

$$\begin{aligned} \frac{d^2 \hat{w}}{dz^2} + \frac{2ik_y f_v (U' + f_h)}{\sigma^2 + f_v^2} \frac{d\hat{w}}{dz} \\ - \left[k_y^2 \frac{\sigma^2 + N^2 + f_h (U' + f_h)}{\sigma^2 + f_v^2} - \frac{ik_y f_v U''}{\sigma^2 + f_v^2} \right] \hat{w} = 0. \end{aligned} \quad (39)$$

To the above ODE, we apply the WKBJ approximation

$$\hat{w} \sim \exp \left[\frac{1}{\delta} \sum_{l=0} \delta^l K_l(z) \right], \quad (40)$$

(see also, Park et al. 2020, 2021). At the leading order, we find that the small parameter δ scales as $\delta = k_y^{-1}$ and the leading-order function $K_0(z)$ satisfies the following relation:

$$K_0' = -\frac{if_v (U' + f_h)}{\sigma^2 + f_v^2} \pm \sqrt{\frac{\sigma^2 + N^2 + f_h (U' + f_h)}{\sigma^2 + f_v^2} - \frac{f_v^2 (U' + f_h)^2}{(\sigma^2 + f_v^2)^2}}. \quad (41)$$

We recall that $'$ denotes the derivative with respect to z . To express the WKBJ solutions more concisely, we define the function Δ

$$\Delta = \frac{\sigma^2 + N^2 + f_h (U' + f_h)}{\sigma^2 + f_v^2} - \frac{f_v^2 (U' + f_h)^2}{(\sigma^2 + f_v^2)^2}. \quad (42)$$

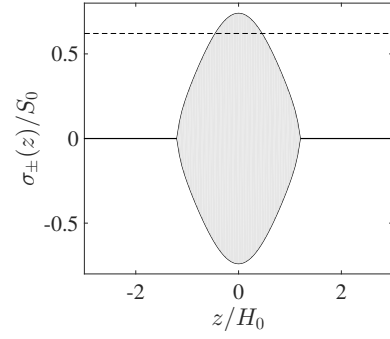


Figure 6. Epicyclic growth rates σ_{\pm} (solid lines) for $R_v = 1$, $R_h = \infty$, and $Ri = 0.1$. White and grey areas denote the regions where $\Delta(z)$ is positive and negative (i.e. the WKBJ solution is evanescent-like and wavelike), respectively. The dashed line indicates the growth rate $\sigma/S_0 = 0.6206$ at $k_x = 0$ and $k_y H_0 = 5$.

On the one hand, when $\Delta(z) > 0$, we expand \hat{w} as

$$\begin{aligned} \hat{w} = \exp \left[-\frac{ik_y f_v (U + f_h z)}{\sigma^2 + f_v^2} \right] \times \\ \left[A_+ \exp \left(k_y \int_z \sqrt{\Delta} dz \right) + A_- \exp \left(-k_y \int_z \sqrt{\Delta} dz \right) \right] + O(1), \end{aligned} \quad (43)$$

where A_+ and A_- are the constant amplitudes to be determined by the boundary conditions. The prefactor \mathcal{P} defined as

$$\mathcal{P} = \exp \left[-\frac{ik_y f_v (U + f_h z)}{(\sigma^2 + f_v^2)} \right], \quad (44)$$

in the above equation (43) implies that the mode shape \hat{w} is not completely evanescent but has a wavelike behaviour if $f_v \neq 0$. The next-order term of $O(1)$ will be neglected in the analysis. On the other hand, if $\Delta(z) < 0$, the mode shape \hat{w} is wavelike at the leading order as

$$\begin{aligned} \hat{w} = \exp \left[-\frac{ik_y f_v (U + f_h z)}{\sigma^2 + f_v^2} \right] \times \\ \left[B_+ \exp \left(ik_y \int_z \sqrt{-\Delta} dz \right) + B_- \exp \left(-ik_y \int_z \sqrt{-\Delta} dz \right) \right], \end{aligned} \quad (45)$$

where B_+ and B_- are constants.

The two solutions (43) and (45) are distinguishable by the sign of Δ . Around the turning points z_t where $\Delta(z_t) = 0$, the solutions (43) and (45) are no longer valid and we need to derive local solutions around the turning points to connect these two WKBJ solutions. We facilitate this turning point analysis by substituting \hat{w} with a new variable $\hat{W} = \hat{w}/\mathcal{P}$ and implementing \hat{W} into (39) to obtain the following second-order ODE at the leading order:

$$\frac{d^2 \hat{W}}{dz^2} - k_y^2 \Delta \hat{W} = 0. \quad (46)$$

From (46), we clearly see that \hat{W} can be expressed as an evanescent solution when $\Delta > 0$:

$$\hat{W} = A_+ \exp \left(k_y \int_z \sqrt{\Delta} dz \right) + A_- \exp \left(-k_y \int_z \sqrt{\Delta} dz \right), \quad (47)$$

or a wavelike solution when $\Delta < 0$:

$$\hat{W} = B_+ \exp \left(ik_y \int_z \sqrt{-\Delta} dz \right) + B_- \exp \left(-ik_y \int_z \sqrt{-\Delta} dz \right). \quad (48)$$

To figure out where turning points z_t at which $\Delta(z = z_t) = 0$ are located at given parameters, it is practical to introduce the epicyclic growth rates $\sigma_{\pm}(z)$ defined as

$$\sigma_{\pm}(z) = \pm \sqrt{\frac{-F + \sqrt{F^2 + 4f_v^2 [U'(U' + f_h) - N^2]}}{2}} \quad (49)$$

where $F(z) = f_v^2 + N^2 + f_h(U'(z) + f_h)$ (see also, [Park 2012](#); [Park et al. 2017](#)). The epicyclic growth rates σ_{\pm} are obtained after replacing σ by σ_{\pm} in Δ to locate where $\Delta = 0$ at a given σ . For instance, in Fig. 6, the growth rate $\sigma/S_0 = 0.6206$ (horizontal dashed line), which is obtained for the parameters $R_v = 1$, $R_h = \infty$, $Ri = 0.1$, $\nu_0 = \kappa_0 = k_x = 0$, and $k_y H_0 = 5$, crosses the epicyclic growth rate $\sigma_+(z)$ at $z/H_0 = \pm 0.453$ and these are the corresponding turning points $z_{t\pm}$. The bounded grey region where $\sigma_- < \sigma < \sigma_+$ denotes the regime where $\Delta(z) < 0$, while the regions $\sigma > \sigma_+(z)$ and $\sigma < \sigma_-(z)$ denote the regimes where $\Delta(z) > 0$. Therefore, for the growth rate $\sigma/S_0 = 0.6206$, the WKB solution of \hat{W} is evanescent when $|z/H_0| > 0.453$ and is wavelike when $|z/H_0| < 0.453$. This configuration in which the wavelike solution is bounded by evanescent solutions can construct an eigenfunction that satisfies the exponentially-decaying solution as $|z| \rightarrow \infty$ ([Le Dizès & Lacaze 2005](#)). This implies that the eigenfunction can be constructed if the growth rate lies in the range $\min(\sigma_-) < \sigma < \max(\sigma_+)$. One of the advantages in using the epicyclic growth rates is that we can easily figure out the growth rate ranges in which the eigenfunction can exist for various sets of parameters of (R_v, R_h) prior to actual stability computation.

For the case with the growth rate lying in the range $\min(\sigma_-) < \sigma < \max(\sigma_+)$, we construct the eigenfunction as follows. We have the two turning points $z_{t\pm}$ where $z_{t+} > z_{t-}$. For $z > z_{t+}$, we consider a solution that decays exponentially as $z \rightarrow \infty$:

$$\hat{W} = A_+ \exp\left(-k_y \int_{z_{t+}}^z \sqrt{\Delta(l)} dl\right). \quad (50)$$

Around the turning point $z = z_{t+}$ where the WKB approximation (50) is no longer valid, we can find a local solution using the following equation obtained by expanding the ODE (46) around a new coordinate $z_{\epsilon} = (z - z_{t+})/\epsilon$ with a small parameter ϵ :

$$\frac{d^2 \hat{W}}{dz_{\epsilon}^2} - \epsilon^3 k_y^2 \Delta'_{t+} z_{\epsilon} \hat{W} = 0, \quad (51)$$

where $\Delta'_{t+} = \Delta'(z_{t+})$ is the vertical gradient of Δ evaluated at $z = z_{t+}$. By taking $\epsilon = \left(k_y^2 \Delta'_{t+}\right)^{-1/3}$, the local equation (51) becomes the Airy equation and \hat{W} can be expressed as the sum of the Airy functions:

$$\hat{W} = a_1 \text{Ai}(z_{\epsilon}) + b_1 \text{Bi}(z_{\epsilon}), \quad (52)$$

where a_1 and b_1 are constants ([Abramowitz & Stegun 1972](#)). Considering the asymptotic behaviors of the Airy functions as $z_{\epsilon} \rightarrow \pm\infty$ and matching the local solution (52) in the limits $z_{\epsilon} \rightarrow \pm\infty$ with the WKB solution (50) in the limit $z \rightarrow z_{t+}$, we impose $b_1 = 0$ and find the wavelike WKB solution in the region $z_{t-} < z < z_{t+}$ as

$$\hat{W} = B_+ \exp\left(ik_y \int_z^{z_{t+}} \sqrt{-\Delta(l)} dl\right) + B_- \exp\left(-ik_y \int_z^{z_{t+}} \sqrt{-\Delta(l)} dl\right), \quad (53)$$

where the constants B_{\pm} satisfy

$$B_+ = \exp\left(-i\frac{\pi}{4}\right) A_+ \quad \text{and} \quad B_- = \exp\left(i\frac{\pi}{4}\right) A_+ \quad (54)$$

(see also, [Olver 1974](#)). We re-write the solution (53) as

$$\hat{W} = C_+ \exp\left(ik_y \int_{z_{t-}}^z \sqrt{-\Delta(l)} dl\right) + C_- \exp\left(-ik_y \int_{z_{t-}}^z \sqrt{-\Delta(l)} dl\right), \quad (55)$$

where C_+ and C_- are constants that are phase-shifted from B_+ and B_- with satisfying the following relation:

$$\frac{B_-}{C_+} = \frac{C_-}{B_+} = \exp\left(ik_y \int_{z_{t-}}^{z_{t+}} \sqrt{-\Delta(l)} dl\right). \quad (56)$$

A similar turning point analysis can be performed around the turning point z_{t-} to connect the WKB solution (55) in the region $z_{t-} < z < z_{t+}$ and the WKB solution in the region $z < z_{t-}$ decaying exponentially as $z \rightarrow -\infty$:

$$\hat{W} = A_- \exp\left(-k_y \int_z^{z_{t-}} \sqrt{\Delta(l)} dl\right). \quad (57)$$

The connection between the two solutions (57) and (55) via the local turning point analysis around $z = z_{t-}$ leads to the following quantization condition:

$$k_y \int_{z_{t-}}^{z_{t+}} \sqrt{-\Delta(z)} dz = \left(m - \frac{1}{2}\right) \pi, \quad (58)$$

where m denotes the mode number as a positive integer (i.e. $m = 1, 2, \dots$). The quantization condition (58) implies that there are modes with different number of oscillations between the turning points $z_{t\pm}$ depending on the mode number m . Eq. (58) can be used directly to compute the growth rate σ in an implicit way ([Billant & Le Dizès 2009](#); [Park & Billant 2013b](#)). However, we can further expand (58) to express σ more explicitly in terms of other parameters. We note that the right-hand-side term of (58) is finite and independent of k_y and thus the left-hand-side term should remain finite as k_y increases. This implies that the integral on the left-hand side is of order $O(k_y^{-1})$ and the turning points $z_{t\pm}$ should approach each other to allow the integral becomes zero as $k_y \rightarrow \infty$. As the turning points are symmetric to $z = 0$, the two turning points behave as $z_{t+} \rightarrow 0$ and $z_{t-} \rightarrow 0$ as k_y increases. Considering this behavior and following previous studies by [Billant & Gallaire \(2005\)](#); [Park & Billant \(2013a\)](#); [Park et al. \(2021\)](#), we use the Taylor expansion of the growth rate σ :

$$\sigma = \sigma_0 - \frac{\sigma_1}{k_y} + O\left(\frac{1}{k_y^2}\right), \quad (59)$$

and apply (59) to the quantization condition (58) after expanding it around $z = 0$. This leads to the following leading-order growth rate σ_0 and the first-order term σ_1 as

$$\sigma_0 = \sqrt{\frac{-F_0 + \sqrt{F_0^2 + 4f_v^2 [S_0(S_0 + f_h) - N^2]}}{2}}, \quad (60)$$

where $F_0 = f_v^2 + N^2 + f_h(S_0 + f_h)$ and

$$\sigma_1 = \left(m - \frac{1}{2}\right) \frac{(\sigma_0^2 + f_v^2) \sqrt{2S_0 [f_v^2 (f_h + 2S_0) - f_h \sigma_0^2]}}{\sqrt{2} \sigma_0 H_0 [2\sigma_0^2 + N^2 + f_v^2 + f_h(S_0 + f_h)]}. \quad (61)$$

The term σ_1 is positive, which implies that $\sigma = \sigma_0$ obtained as $k_y \rightarrow \infty$ is the maximum growth rate.

Figure 7 shows examples of the growth rates σ as a function of the wavenumber k_y for various parameters Ri , Ω_0 and θ at $k_x = \nu_0 = \kappa_0 = 0$. Numerical results (lines) have a very good agreement with

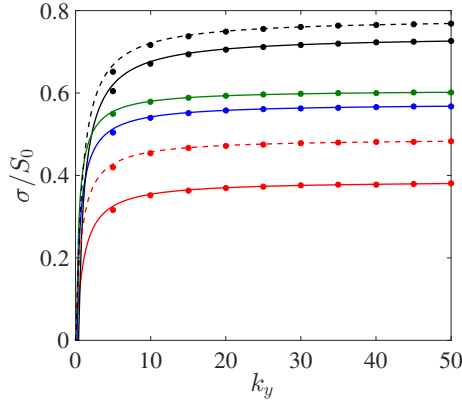


Figure 7. Growth rate σ versus wavenumber k_y at $k_x = \nu_0 = \kappa_0 = 0$ for various sets of parameters $(Ri, \Omega_0/S_0, \theta)$; from top to bottom, $(0.01, 0.5, 0^\circ)$ (black dashed), $(0.1, 0.5, 0^\circ)$ (black solid), $(0.1, 0.5, 45^\circ)$ (green solid), $(0.1, 0.25, 180^\circ)$ (blue solid), $(0.01, -0.25, 90^\circ)$ (red dashed), and $(0.1, -0.25, 90^\circ)$ (red solid). Filled circles denote predictions from the WKB asymptotic dispersion relation (59).

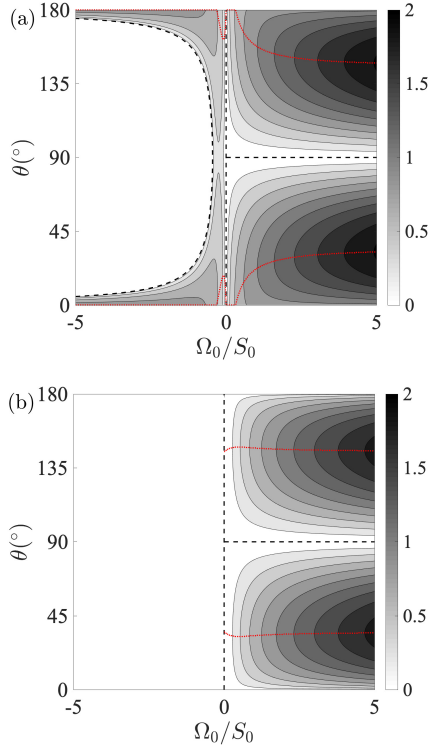


Figure 8. The maximum growth rate σ_0/S_0 (60) in the parameter space (Ω_0, θ) for (a) $Ri = 0.1$ and (b) $Ri = 1$. Black dashed lines indicate the stability thresholds where the growth rate σ_0 becomes zero. Red dotted lines denote the co-latitude θ at which the local maximum growth rate is.

the WKB predictions from (59) (filled circles). For all parameters, we see that the growth rate increases with k_y and asymptotes to the predicted maximum growth rate σ_0 as $k_y \rightarrow \infty$. At fixed Ω_0 and θ , the growth-rate curves descend as Ri increases. This indicates the stabilizing role of the stratification as similarly reported in previous studies on horizontal-shear inertial instability (Arobone & Sarkar 2012; Park et al. 2021).

Results like growth-rate curves as a function of the wavenumber

k_y in Fig. 7 can explain the effects of various parameters but in a limited way. To better understand parametric dependence of the growth rate, we display in Fig. 8 contours of the maximum growth rate σ_0 of (60) in the parameter space (Ω_0, θ) for two values of Ri : $Ri = 0.1$ and $Ri = 1$. For both cases, we see that the growth rate is larger in the cyclonic regime $\Omega_0/S_0 > 0$ where the signs of the star's rotation Ω_0 and the shear S_0 are the same. For $Ri = 0.1$ in panel a, the maximum of σ_0 is found at the poles: $\theta = 0^\circ$ and 180° for slow rotation $0 < \Omega_0/S_0 < 0.31$. For fast rotation $\Omega_0/S_0 > 0.31$, σ_0 is maximal not at the poles but at colatitudes in the ranges: $0^\circ < \theta < 40^\circ$ or $140^\circ < \theta < 180^\circ$. For stronger stratification with $Ri = 1$ in panel b, the maximum of σ_0 is found near the co-latitudes $\theta = 40^\circ$ and 140° for any cyclonic rotation $\Omega_0/S_0 > 0$. In the anti-cyclonic regime $\Omega_0/S_0 < 0$ where the signs of the star's rotation Ω_0 and the shear S_0 are the opposite, the inertial instability is much more suppressed than the instability in the cyclonic regime. For the weakly stratified case $Ri = 0.1$, the maximum of σ_0 is found near the poles in the ranges: $0^\circ < \theta < 18^\circ$ and $162^\circ < \theta < 180^\circ$ for slow anti-cyclonic rotation $-0.31 < \Omega_0/S_0 < 0$ while the maximum is found at the poles $\theta = 0^\circ$ and 180° for fast anti-cyclonic rotation $\Omega_0/S_0 < -0.31$. At the equator $\theta = 90^\circ$, which corresponds to the case under the traditional f -plane approximation, we see that it is unstable only in the narrow range $-0.25 < \Omega_0/S_0 < 0$ and stable elsewhere for $Ri = 0.1$. For $Ri \geq 1$, no instability is found in the anti-cyclonic regime $\Omega_0/S_0 < 0$ at any latitude.

Figure 8 clearly shows that the cyclonic rotation can significantly promote the inertial instability at the poles or away from the poles depending on its magnitude Ω_0/S_0 while the anticyclonic rotation with $\Omega_0/S_0 < 0$ promotes weak inertial instability near the poles or no instability if the stratification is strong enough. The complete rotation effect by the full Coriolis acceleration, which is applicable at any latitude, has not been thoroughly considered in previous studies on vertical shear instabilities in rotating fluids. For instance, the traditional approximation of rotation (TAR; see also Mathis & Prat 2019; Dhouib et al. 2021) neglecting the horizontal component of the rotation vector cannot predict the instability around the equator $\theta = 90^\circ$. Our results bring attention to the importance of the full Coriolis acceleration on the inertial instability, as the instability of vertically-sheared flows is strong especially near the mid latitudes $\theta = 45^\circ$ or $\theta = 135^\circ$, which cannot be properly captured by the traditional approach.

4.2 WKBJ analysis in the high-diffusivity limit $\kappa_0 \rightarrow \infty$

We now consider the opposite limit $\kappa_0 \rightarrow \infty$ (i.e., $Pe \rightarrow 0$) where the thermal diffusion is strong, a situation more relevant to the interior of stars. For $k_x = 0$ at which the inertial instability has the maximum growth, the 4th-order ODE (36) can be re-written as

$$\begin{aligned} & \frac{d^4 \hat{w}}{dz^4} + \frac{ik_y f_v (U' + 2f_h)}{f_v^2 + \sigma^2} \frac{d^3 \hat{w}}{dz^3} \\ & - \frac{k_y^2 [2\sigma^2 + f_v^2 + f_h(U' + f_h)] - 3ik_y f_v U'''}{f_v^2 + \sigma^2} \frac{d^2 \hat{w}}{dz^2} \\ & - \frac{ik_y^3 f_v (U' + 2f_h) + 2k_y^2 f_h U'''}{f_v^2 + \sigma^2} \frac{d \hat{w}}{dz} \\ & + \frac{k_y^4 [\sigma^2 + f_h(U' + f_h)] - ik_y^3 f_v U'' - k_y^2 f_h U'''}{f_v^2 + \sigma^2} \hat{w} \\ & = O\left(\frac{1}{\kappa_0}\right). \end{aligned} \quad (62)$$

We neglect the terms of the order of $O(\kappa_0^{-1})$ for large κ_0 and consider only the leading-order terms for large k_y to apply the WKBJ approximation. The above ODE (62) is then simplified as

$$\begin{aligned} \frac{d^4 \hat{w}}{dz^4} + \frac{ik_y f_v (U' + 2f_h)}{f_v^2 + \sigma^2} \frac{d^3 \hat{w}}{dz^3} \\ - \frac{k_y^2 [2\sigma^2 + f_v^2 + f_h (U' + f_h)]}{f_v^2 + \sigma^2} \frac{d^2 \hat{w}}{dz^2} - \frac{ik_y^3 f_v (U' + 2f_h)}{f_v^2 + \sigma^2} \frac{d\hat{w}}{dz} \\ + \frac{k_y^4 [\sigma^2 + f_h (U' + f_h)]}{f_v^2 + \sigma^2} \hat{w} = 0. \end{aligned} \quad (63)$$

If we apply the same WKBJ approximation (40), we find that $\delta = k_y^{-1}$ and the leading-order function $K_0(z)$ satisfies the following 4th-order polynomial equation:

$$K_0'^4 + \mathcal{K}_1 K_0'^3 - (1 + \mathcal{K}_2) K_0'^2 - \mathcal{K}_1 K_0' + \mathcal{K}_2 = 0, \quad (64)$$

where

$$\mathcal{K}_1 = \frac{if_v (U' + 2f_h)}{\sigma^2 + f_v^2}, \quad \mathcal{K}_2 = \frac{\sigma^2 + f_h (U' + f_h)}{\sigma^2 + f_v^2}. \quad (65)$$

The quartic equation (64) has four solutions

$$K_0' = \pm 1, \quad K_0' = \frac{-\mathcal{K}_1 \pm \sqrt{\mathcal{K}_1^2 + 4\mathcal{K}_2}}{2}. \quad (66)$$

The first two WKBJ solutions with $K_0' = \pm 1$ imply that $\hat{w} \simeq a_+ \exp(k_y z) + a_- \exp(-k_y z)$ and thus we have $a_{\pm} = 0$ after considering the boundary conditions that decay exponentially as $z \rightarrow \pm\infty$. The remaining WKBJ solutions are

$$\begin{aligned} \hat{w} = \exp \left[-\frac{ik_y f_v (U + 2f_h z)}{2(\sigma^2 + f_v^2)} \right] \times \\ \left[C_+ \exp \left(k_y \int_z \sqrt{\Gamma} dz \right) + C_- \exp \left(-k_y \int_z \sqrt{\Gamma} dz \right) \right], \end{aligned} \quad (67)$$

where

$$\Gamma = \frac{\sigma^2 + f_h (U' + f_h)}{\sigma^2 + f_v^2} - \frac{f_v^2 (U' + 2f_h)^2}{4(\sigma^2 + f_v^2)^2}. \quad (68)$$

Similar to the WKBJ analysis in the previous subsection, we facilitate the turning point analysis by introducing a new variable $\hat{V} = \hat{w}/Q$ where Q is the prefactor on the right-hand side term in (67)

$$Q = \exp \left[-\frac{ik_y f_v (U + 2f_h z)}{2(\sigma^2 + f_v^2)} \right]. \quad (69)$$

For the variable \hat{V} , we find the following 4th-order ODE at the leading order:

$$\begin{aligned} \frac{d^4 \hat{V}}{dz^4} - \frac{ik_y f_v (U' + 2f_h)}{f_v^2 + \sigma^2} \frac{d^3 \hat{V}}{dz^3} \\ - \frac{k_y^2 [2\sigma^2 + f_v^2 + f_h (U' + f_h)]}{f_v^2 + \sigma^2} \frac{d^2 \hat{V}}{dz^2} + \frac{ik_y^3 f_v (U' + 2f_h) \Gamma}{\sigma^2 + f_v^2} \frac{d\hat{V}}{dz} \\ + k_y^4 \Gamma \left[1 + \frac{f_v^2 (U' + 2f_h)^2}{4(\sigma^2 + f_v^2)^2} \right] \hat{V} = O \left(\frac{1}{k_y} \right). \end{aligned} \quad (70)$$

The WKBJ solution for \hat{V} can be expressed as an evanescent solution if $\Gamma > 0$:

$$\hat{V} = D_+ \exp \left(k_y \int_z \sqrt{\Gamma} dz \right) + D_- \exp \left(-k_y \int_z \sqrt{\Gamma} dz \right), \quad (71)$$

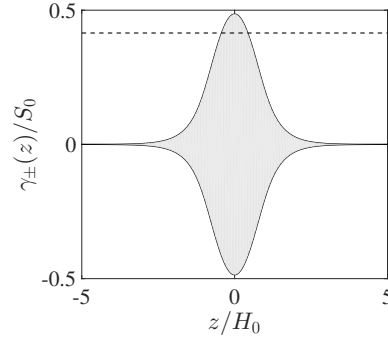


Figure 9. Epicyclic growth rates γ_{\pm} (solid lines) for $\Omega_0/S_0 = -0.25$ and $\theta = 45^\circ$. White and grey areas denote the regions where $\Gamma(z)$ is positive and negative, i.e. the WKBJ solution is evanescent-like and wavelike, respectively. The dashed line indicates the growth rate $\sigma/S_0 = 0.415$ numerically obtained for $Pe = 0.01$ at $(k_x H_0, k_y H_0) = (0, 5)$.

or a wavelike solution if $\Gamma < 0$:

$$\hat{V} = E_+ \exp \left(ik_y \int_z \sqrt{-\Gamma} dz \right) + E_- \exp \left(-ik_y \int_z \sqrt{-\Gamma} dz \right), \quad (72)$$

where D_{\pm} and E_{\pm} are constants to be determined by the boundary conditions.

To find turning points z_t where $\Gamma = 0$, we define the epicyclic growth rates γ_{\pm} :

$$\gamma_{\pm}(z) = \pm \sqrt{\frac{-F_1 + \sqrt{F_1^2 + f_v^2 U'^2}}{2}} \quad (73)$$

where $F_1(z) = f_v^2 + f_h (U'(z) + f_h)$. Figure 9 shows an example of the epicyclic growth rate γ_{\pm} for the parameters $\Omega_0/S_0 = -0.25$ and $\theta = 45^\circ$. The profiles of γ_{\pm} are similar to those of $\sigma_{\pm}(z)$ in Fig. 6 such that γ_+ and γ_- reaches their maximum and minimum at $z = 0$, respectively, due to their symmetry at $z = 0$. The use of the epicyclic growth rate γ_{\pm} is the same as that of σ_{\pm} : the solution is wavelike if the growth rate σ is in the range $\gamma_- < \sigma < \gamma_+$ while it is evanescent if $\sigma > \gamma_+$ or $\sigma < \gamma_-$. For the growth rate $\sigma/S_0 = 0.415$, which is computed numerically at $Pe = 0.01$ and $(k_x H_0, k_y H_0) = (0, 5)$, the turning points are at $z_{t\pm} = \pm 0.43 H_0$ and we can view from the WKBJ analysis that the eigenfunction is evanescent for $|z/H_0| > 0.43$ while it is wavelike in the region $-0.43 < z/H_0 < 0.43$.

The eigenfunction can be constructed as follows. We first consider an exponentially-decaying solution in the region $z > z_{t+}$:

$$\hat{V} = D_+ \exp \left(-k_y \int_{z_{t+}}^z \sqrt{\Gamma(l)} dl \right), \quad (74)$$

where D_+ is a constant. The WKBJ solution (74) for $z > z_{t+}$ can be connected with the WKBJ solution for $z < z_{t+}$ by considering the local equation around z_{t+} with a new local variable $z_{\epsilon} = (z - z_{t+})/\epsilon$ with small ϵ and the Taylor expansion $\Gamma \simeq \Gamma'_{t+} \epsilon z_{\epsilon}$:

$$\frac{d^2 \hat{V}}{dz_{\epsilon}^2} - z_{\epsilon} \hat{V} = O \left(\frac{1}{k_y^{1/3}} \right), \quad (75)$$

where we consider the small parameter $\epsilon = (k_y^2 \Gamma'_{t+})^{-2/3}$. Neglecting the terms of order $O(k_y^{-1/3})$ on the right-hand side, we recover the Airy equation for \hat{V} . By considering the asymptotic behaviors of the Airy functions $\hat{V}(z_{\epsilon}) = c_1 \text{Ai}(z_{\epsilon}) + d_1 \text{Bi}(z_{\epsilon})$ in the limit $z_{\epsilon} \rightarrow \pm\infty$,

we find the following WKBJ solution in the region $z_{t-} < z < z_{t+}$:

$$\hat{W} = E_+ \exp\left(ik_y \int_z^{z_{t+}} \sqrt{-\Gamma(l)} dl\right) + E_- \exp\left(-ik_y \int_z^{z_{t+}} \sqrt{-\Gamma(l)} dl\right), \quad (76)$$

where constants E_{\pm} satisfy

$$E_+ = \exp\left(-i\frac{\pi}{4}\right) D_+, \quad E_- = \exp\left(i\frac{\pi}{4}\right) D_+. \quad (77)$$

The similar analysis as in the previous subsection can be done to connect the WKBJ solution (76) in the region $z_{t-} < z < z_{t+}$ with an exponentially-decaying solution in the region $z < z_{t-}$:

$$\hat{V} = D_+ \exp\left(k_y \int_{z_{t-}}^z \sqrt{\Gamma(l)} dl\right). \quad (78)$$

The turning point analysis leads to the following quantization condition:

$$k_y \int_{z_{t-}}^{z_{t+}} \sqrt{-\Gamma(z)} dz = \left(m - \frac{1}{2}\right) \pi, \quad (79)$$

where m is the mode number. Same as in (59), we can apply the Taylor expansion of Γ around $z = 0$ and express the growth rate σ as

$$\sigma = \gamma_0 - \frac{\gamma_1}{k_y} + O\left(\frac{1}{k_y^2}\right), \quad (80)$$

where γ_0 is the leading-order term

$$\gamma_0 = \sqrt{\frac{-f_v^2 - f_h(S_0 + f_h) + \sqrt{[f_v^2 + (S_0 + f_h)^2] (f_v^2 + f_h^2)}}{2}}, \quad (81)$$

and γ_1 is the first-order term of the expansion (80)

$$\gamma_1 = \left(m - \frac{1}{2}\right) \frac{(\gamma_0^2 + f_v^2) \sqrt{2S_0 [f_v^2 S_0 - 2f_h \gamma_0^2]}}{\gamma_0 H_0 [4\gamma_0^2 + 2f_v^2 + 2f_h(S_0 + f_h)]}. \quad (82)$$

The leading-order term γ_0 corresponds to the maximum growth rate obtained in the limit $k_y \rightarrow \infty$ since $\gamma_1 > 0$. We see in Fig. 5 that the asymptotic growth rates from (80) show very good agreement with numerical results for a highly diffusive case with $Pe = 0.01$, especially when k_y is sufficiently large.

The advantage of using analytic expressions such as the growth rate (80) or the maximum growth rate (81) is that we can easily undertake parametric investigations on the growth rate in the space (Ω_0, θ) as shown in Fig. 10. For cyclonic rotation with $\Omega_0/S_0 > 0$, the maximum of γ_0 is attained at the poles $\theta = 0^\circ$ and 180° . At the equator $\theta = 90^\circ$ (i.e. $f_v = 0$, $f_h = 2\Omega_0$), the maximum growth rate γ_0 is positive only in a narrow anti-cyclonic range of $-0.5 < \Omega_0/S_0 < 0$ since $\gamma_0 = \sqrt{-2\Omega_0(S_0 + 2\Omega_0)}$ and the maximum of γ_0 is attained at $\Omega_0/S_0 = -0.25$ as $\gamma_{0,\max} = S_0/2$. In the anti-cyclonic rotation regime $\Omega_0/S_0 < 0$, $\gamma_{0,\max}$ outside the equator is attained below $\Omega_0/S_0 = -0.25$ and γ_0 is higher near the poles.

We note that the contours of the maximum growth rate σ_0 for the non-diffusive case $\kappa_0 = 0$ shown in Fig. 8 are quite different from those in the high-diffusivity limit $\kappa_0 \rightarrow \infty$ shown in Fig. 10, the latter which are more relevant to the stellar radiation zones with high thermal diffusive fluids. The non-diffusive case has the maximum instability in the middle latitudes (i.e. co-latitudes around $\theta = 45^\circ$ or $\theta = 135^\circ$) while the highly-diffusive case has the maximum instability around the poles (i.e. $\theta = 0^\circ$ or $\theta = 180^\circ$). It is also noteworthy that

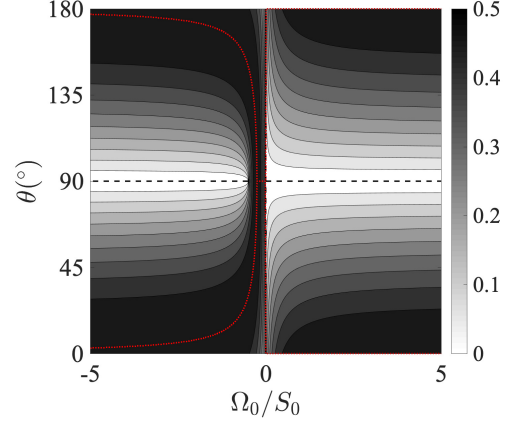


Figure 10. The maximum growth rate γ_0/S_0 (81) in the parameter space (Ω_0, θ) . Black dashed lines indicate contour lines on which the growth rate becomes zero. Red dotted lines indicate the co-latitude θ at which γ_0 is locally maximal.

in the high-diffusivity limit $\kappa_0 \rightarrow \infty$, our finding on the inertial instability of vertical shear flow is different from that of horizontal shear flow where the growth rate is maximum near the equator $\theta = 90^\circ$ (Park et al. 2021). This emphasizes the importance of understanding carefully the role of the full Coriolis acceleration in deriving the instability and turbulence in the radiation zones in stellar interiors.

Figures 8 and 10 show the strong latitudinal dependence of the growth rate of the inertial instability. As in the case of the inflectional instability, we can therefore expect regions where the turbulent energy dissipation, momentum transport, and matter mixing will be localised. For instance, the inertial instability will trigger turbulent transport in the polar regions while it will vanish around the equator in the stellar regime with strong heat diffusion.

4.3 Characteristic time scale of turbulent dissipation induced by inertial instability

While inflectional instability is difficult to treat analytically, we derived in the previous subsections analytical expressions of the growth rate for the inertial instability. Using these expressions, we can further deduce a scaling law for the characteristic time scale of turbulent dissipation induced by the inertial instability. We first consider the shellular rotation of stars varying with radius (i.e. $\Omega = \Omega(r)$). In the local frame rotating with Ω_0 at r , we have the relative azimuthal velocity U :

$$U = r \sin \theta (\Omega - \Omega_0), \quad (83)$$

and its radial gradient reads

$$\frac{\partial U}{\partial r} = \sin \theta \left(\Omega + r \frac{\partial \Omega}{\partial r} - \Omega_0 \right). \quad (84)$$

At given co-latitude θ and radius r , we rewrite the radial gradient in terms of the local vertical shear S_0 :

$$S_0(\epsilon) = \epsilon 2\Omega_0 \sin \theta, \quad (85)$$

where $\epsilon(r)$ is the nondimensional shear parameter defined as

$$\epsilon(r) = \frac{1}{2\Omega_0} \frac{\partial}{\partial r} [r (\Omega - \Omega_0)]. \quad (86)$$

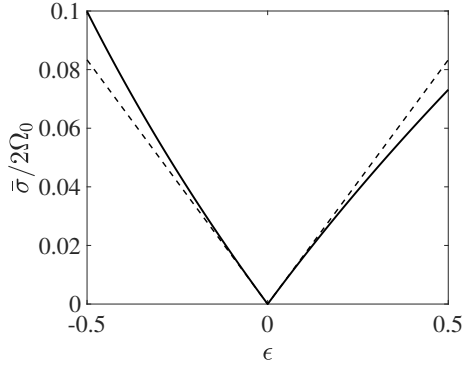


Figure 11. The average growth rate $\bar{\sigma}$ (88) as a function of ϵ (solid line) and its small- ϵ linear approximation (89) (dashed line).

By putting S_0 into the maximum growth rate (81) in the high-diffusivity limit $\kappa_0 \rightarrow \infty$, we retain the following expression:

$$\frac{\sigma^2}{(2\Omega_0)^2} = \frac{\sqrt{(\epsilon^2 + 2\epsilon) \sin^2 \theta + 1} - 1 - \epsilon \sin^2 \theta}{2}. \quad (87)$$

The above expression (87) implies that the growth rate σ is always positive except at the poles (i.e. $\sin \theta = 0$) and equator (i.e. $\sin \theta = 1$).

We can consider a latitudinally-averaged growth rate $\bar{\sigma}$ defined as

$$\bar{\sigma} = \frac{1}{2} \int_0^\pi \sigma \sin \theta d\theta, \quad (88)$$

(see also, Chaboyer & Zahn 1992). Figure 11 shows how $\bar{\sigma}$ varies with ϵ . The symmetry with respect to $\epsilon = 0$ breaks down as $|\epsilon|$ increases. However, in the limit $|\epsilon| \rightarrow 0$, we can expand $\bar{\sigma}$ using the Taylor expansion and find a linear relation as

$$\frac{\bar{\sigma}}{2\Omega_0} \approx \frac{1}{6} |\epsilon|, \quad (89)$$

where the prefactor $1/6$ is obtained analytically by considering a small- ϵ limit.

If we assume that turbulence in the stellar interior is generated dominantly by the vertical shear instability, we can consider the viscosity ratio as

$$\frac{\bar{v}_{v,v}}{\bar{v}_{h,v}} = \frac{l_{\parallel}^2}{l_{\perp}^2}, \quad (90)$$

where l_{\parallel} and l_{\perp} are the characteristic length scales of turbulence in the directions parallel and perpendicular to the stratification, respectively (i.e. vertical and horizontal directions; see also, Mathis et al. 2018). The dynamical time scale τ characterizing the turbulence induced by the vertical shear instability follows the scaling law as an inverse of the growth rate $\bar{\sigma}$:

$$\tau = \frac{l_{\perp}^2}{\bar{v}_{h,v}} = \frac{l_{\parallel}^2}{\bar{v}_{v,v}} = \frac{1}{\bar{\sigma}} \approx \frac{6}{2\Omega_0 |\epsilon|}. \quad (91)$$

A scaling law for the characteristic time scale τ is similarly derived in the context of turbulence induced by the horizontal shear instability in Park et al. (2021).

5 LINK BETWEEN INERTIAL AND SYMMETRIC INSTABILITIES

The inertial instability as well as the Goldreich-Schubert-Fricke (GSF) instability (Barker et al. 2020) are closely related to another

type of instability called the symmetric instability, which has been studied mainly in the context of geophysics (e.g., slantwise convection; see also Holton 2004). Recent studies by Tort et al. (2016) and Zeitlin (2018) revealed that the full Coriolis acceleration can promote the symmetric instability, similar to what this paper claims for the inertial instability. In this section, we revisit this symmetric instability problem without taking any assumption on thermal diffusivity (e.g., $Pr = \nu_0/\kappa_0 = 1$ in the case of Zeitlin (2018)) and aim to demonstrate mathematically that these instabilities are essentially the same even if they are originally derived from different formulations.

To explore the symmetric instability, we consider vertical shear flow with a linear profile as $U = \Lambda z$ where the vertical shear Λ is a constant. We assume that there is no variation in the longitudinal direction x (i.e. $\partial/\partial x = 0$). The linearized perturbation equations are then expressed as

$$\frac{\partial \bar{v}}{\partial y} + \frac{\partial \bar{w}}{\partial z} = 0, \quad (92)$$

$$\frac{\partial \bar{u}}{\partial t} - f_v \bar{v} + (\Lambda + f_h) \bar{w} = \nu_0 \nabla^2 \bar{u}, \quad (93)$$

$$\frac{\partial \bar{v}}{\partial t} + f_v \bar{u} = -\frac{1}{\rho_0} \frac{\partial \bar{p}}{\partial y} + \nu_0 \nabla^2 \bar{v}, \quad (94)$$

$$\frac{\partial \bar{w}}{\partial t} - f_h \bar{u} = -\frac{1}{\rho_0} \frac{\partial \bar{p}}{\partial z} + \alpha_0 g \bar{T} + \nu_0 \nabla^2 \bar{w}, \quad (95)$$

$$\frac{\partial \bar{T}}{\partial t} - \frac{f_v \Lambda}{\alpha_0 g} \bar{v} + \mathcal{T}_{\Theta} \bar{w} = \kappa_0 \nabla^2 \bar{T}. \quad (96)$$

We note that, unlike the case of hyperbolic tangent shear flow, the wide-jet approximation is not required for a linear shear flow as the second derivative U'' is zero and the vertical temperature gradient $\partial \bar{T}/\partial z$ in Eq. (15) becomes constant as $\partial \bar{T}/\partial z = \mathcal{T}_{\Theta}$. For the stability analysis, we consider the following normal mode expression:

$$\left(\bar{u}, \bar{v}, \bar{w}, \bar{p}, \bar{T} \right) = \Re \left[\left(\check{u}, \check{v}, \check{w}, \check{p}, \check{T} \right) \exp(i k_y y + i k_z z + \sigma t) \right], \quad (97)$$

where $\check{u} = (\check{u}, \check{v}, \check{w})$ denotes the perturbation velocity amplitude, \check{p} and \check{T} are normalized amplitudes of the perturbation pressure and temperature, respectively, and k_z is the wavenumber in the vertical direction z . Applying the normal mode (97) to the equations (92)-(96) leads to the following set of equations:

$$i(k_y \check{v} + k_z \check{w}) = 0, \quad (98)$$

$$\sigma \check{u} - f_v \check{v} + (\Lambda + f_h) \check{w} = -\nu_0 k^2 \check{u} \quad (99)$$

$$\sigma \check{v} + f_v \check{u} = -i k_y \check{p} - \nu_0 k^2 \check{v} \quad (100)$$

$$\sigma \check{w} - f_h \check{u} = -i k_z \check{p} + \alpha_0 g \mathcal{T}_{\Theta} \check{T} - \nu_0 k^2 \check{w}, \quad (101)$$

$$\sigma \check{T} - \frac{f_v \Lambda}{\alpha_0 g \mathcal{T}_{\Theta}} \check{v} + \check{w} = -\kappa_0 k^2 \check{T}, \quad (102)$$

where $k^2 = k_y^2 + k_z^2$. From the energy equation (102), we have

$$\check{T} = \left(\frac{f_v \Lambda}{\alpha_0 g \mathcal{T}_{\Theta}} \check{v} - \check{w} \right) / (\sigma + \kappa_0 k^2). \quad (103)$$

From the two momentum equations (100)-(101), we can eliminate the pressure \check{p} and find the relation

$$\begin{aligned} \sigma(k_z\check{v} - k_y\check{w}) &= -(k_y f_h + k_z f_v)\check{u} - \nu_0 k^2(k_z\check{v} - k_y\check{w}) \\ -k_y \alpha_0 g \mathcal{T}_\theta \left(\frac{f_v \Lambda}{\alpha_0 g \mathcal{T}_\theta} \check{v} - \check{w} \right) &/ (\sigma + \kappa_0 k^2). \end{aligned} \quad (104)$$

Using the momentum equation (99) and the continuity equation $\check{w} = -(k_y/k_z)\check{v}$, we find the relation

$$(\sigma + \nu_0 k^2)\check{u} = \left(f_v + \frac{k_y(\Lambda + f_h)}{k_z} \right) \check{v}. \quad (105)$$

Putting these equations into Eq. (104) leads to the following dispersion relation:

$$\begin{aligned} \left[\frac{\sigma k^2}{k_z} + \frac{\nu_0 k^4}{k_z} + \frac{k_y(k_z f_v \Lambda + k_y N^2)}{k_z(\sigma + \kappa_0 k^2)} \right] (\sigma + \nu_0 k^2) \\ + (k_y f_h + k_z f_v) \left(f_v + \frac{k_y(\Lambda + f_h)}{k_z} \right) = 0, \end{aligned} \quad (106)$$

which can further be simplified into the following cubic equation

$$\sigma^3 + A_2 \sigma^2 + A_1 \sigma + A_0 = 0, \quad (107)$$

where

$$\begin{aligned} A_2 &= (2\nu_0 + \kappa_0)k^2, \\ A_1 &= \nu_0(\nu_0 + 2\kappa_0)k^4 \\ &\quad + \frac{k_y(k_z f_v \Lambda + k_y N^2) + (k_y f_h + k_z f_v)[k_z f_v + k_y(\Lambda + f_h)]}{k^2}, \\ A_0 &= \nu_0^2 \kappa_0 k^6 + \nu_0 k_y(k_z f_v \Lambda + k_y N^2) \\ &\quad + \kappa_0(k_z f_v + k_y f_h)[k_z f_v + k_y(\Lambda + f_h)]. \end{aligned} \quad (108)$$

The growth rate σ can be obtained by solving the cubic equation (107). The advantage of the symmetric instability analysis is that both the diffusivity κ_0 and viscosity ν_0 are included in the dispersion relation (107). This allows us to examine explicitly without significant computations on how the viscous and thermal diffusions affect the stability of vertical shear flow in stably stratified-rotating fluids.

For the inviscid case with $\nu_0 = 0$, we can express the growth rate more explicitly. On the one hand, in the low-diffusivity (ld) limit $\kappa_0 \rightarrow 0$, the growth rate σ can be expanded as

$$\sigma = \sigma_{\text{ld}}^{(0)} - \kappa_0 k^2 \sigma_{\text{ld}}^{(1)} + O(\kappa_0^2), \quad (109)$$

where $\sigma_{\text{ld}}^{(0)}$ is the leading-order growth rate

$$\sigma_{\text{ld}}^{(0)} = \frac{1}{k} \sqrt{-k_y(k_z f_v \Lambda + k_y N^2) - (k_y f_h + k_z f_v)[k_z f_v + k_y(\Lambda + f_h)]} \quad (110)$$

and $\sigma_{\text{ld}}^{(1)}$ is the first-order term

$$\sigma_{\text{ld}}^{(1)} = \frac{k_y(k_z f_v \Lambda + k_y N^2)}{2[k_y(k_z f_v \Lambda + k_y N^2) + (k_y f_h + k_z f_v)(k_z f_v + k_y(\Lambda + f_h))]} \quad (111)$$

On the other end, if we take the high-diffusivity (hd) limit $\kappa_0 \rightarrow \infty$, the growth rate σ can be expanded as

$$\sigma = \sigma_{\text{hd}}^{(0)} - \frac{\sigma_{\text{hd}}^{(1)}}{\kappa_0 k^2} + O(\kappa_0^{-2}), \quad (112)$$

where $\sigma_{\text{hd}}^{(0)}$ is the leading-order growth rate in the limit $\kappa_0 \rightarrow \infty$

$$\sigma_{\text{hd}}^{(0)} = \frac{1}{k} \sqrt{-(k_y f_h + k_z f_v)[k_z f_v + k_y(\Lambda + f_h)]} \quad (113)$$

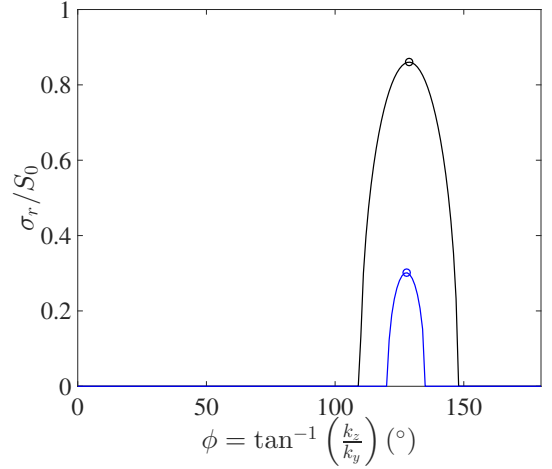


Figure 12. The growth rates $\sigma_{\text{ld}}^{(0)}$ from (116) (black) and $\sigma_{\text{hd}}^{(0)}$ from (117) versus the phase angle ϕ at $\Omega_0/S_0 = 1$, $\theta = 45^\circ$, and $Ri = 0.1$. Black and blue empty circles denote the maxima (119) and (121) at the critical phase angles (118) and (120), respectively.

and $\sigma_{\text{hd}}^{(1)}$ is the first-order term:

$$\sigma_{\text{hd}}^{(1)} = \frac{k_y(k_z f_v \Lambda + k_y N^2)}{2k^2}. \quad (114)$$

The leading-order terms $\sigma_{\text{ld}}^{(0)}$ and $\sigma_{\text{hd}}^{(0)}$ correspond to the growth rates in the limits $\kappa_0 \rightarrow 0$ and $\kappa_0 \rightarrow \infty$, respectively. $\sigma_{\text{ld}}^{(0)}$ and $\sigma_{\text{hd}}^{(0)}$ vary in the wavenumber space (k_y, k_z) and we can find their maxima:

$\max(\sigma_{\text{ld}}^{(0)})$ and $\max(\sigma_{\text{hd}}^{(0)})$ and the corresponding wavenumbers at which the maxima are attained. To simplify the analysis, we introduce a phase angle ϕ between the two wavenumbers k_y to k_z as

$$\phi = \tan^{-1} \left(\frac{k_z}{k_y} \right), \quad (115)$$

where $k_y = k \cos \phi$ and $k_z = k \sin \phi$. By defining the phase angle ϕ , we can express $\sigma_{\text{ld}}^{(0)}$ and $\sigma_{\text{hd}}^{(0)}$ in terms of ϕ as

$$\begin{aligned} \sigma_{\text{ld}}^{(0)} &= \left\{ -\cos^2 \phi [N^2 + f_h(\Lambda + f_h)] - \sin^2 \phi f_v^2 \right. \\ &\quad \left. - 2 \cos \phi \sin \phi f_v (\Lambda + f_h) \right\}^{\frac{1}{2}}, \end{aligned} \quad (116)$$

$$\sigma_{\text{hd}}^{(0)} = \left[-\cos^2 \phi f_h(\Lambda + f_h) - \sin^2 \phi f_v^2 - \cos \phi \sin \phi f_v (\Lambda + 2f_h) \right]^{\frac{1}{2}}. \quad (117)$$

We see that the dependence on the wavenumber magnitude k is eliminated in (116)-(117). In Fig. 12, we display these growth rates at the leading order as a function of the phase angle ϕ at a mid-latitude $\theta = 45^\circ$ for $\Omega_0/S_0 = 1$ and $Ri = 0.1$. For both cases, the growth rates are positive only in a finite range of ϕ and reach their maxima $\max(\sigma_{\text{ld}}^{(0)}) \simeq 0.86$ and $\max(\sigma_{\text{hd}}^{(0)}) \simeq 0.30$ around $\phi \simeq 129^\circ$ and $\phi \simeq 128^\circ$ (i.e. $k_z/k_y = 1.1528$ and $k_z/k_y = 1.1499$), respectively. Such maximum values and critical phase angles can be easily obtained by taking the derivatives with respect to ϕ on the growth rates and finding their zeros (i.e. $\partial\sigma/\partial\phi = 0$). For $\sigma_{\text{ld}}^{(0)}$ in the low-diffusivity limit $\kappa_0 = 0$, we have the critical phase angle $\phi_{c,\text{ld}}$:

$$\phi_{c,\text{ld}} = \tan^{-1} \left[\frac{K_0 - \sqrt{K_0^2 + 4f_v^2(\Lambda + f_h)^2}}{2f_v(\Lambda + f_h)} \right], \quad (118)$$

where $K_0 = f_v^2 - N^2 - f_h(\Lambda + f_h)$, at which the growth rate $\sigma_{\text{ld}}^{(0)}$ reaches its maximum as

$$\max(\sigma_{\text{ld}}^{(0)}) = \sqrt{\frac{-K_1 + \sqrt{K_1^2 + 4f_v^2[(\Lambda + f_h)\Lambda - N^2]}}{2}}, \quad (119)$$

where $K_1 = f_v^2 + N^2 + f_h(\Lambda + f_h)$. We note that this maximum growth rate of the symmetric instability is equivalent to the maximum growth rate (60) for inertial instability obtained by the WKBJ analysis for the non-diffusive case $\kappa_0 = 0$ in the limit $k_y \rightarrow \infty$. Similarly, we can find the critical phase angle and the corresponding maximum of $\sigma_{\text{hd}}^{(0)}$ in the high-diffusivity limit $\kappa_0 \rightarrow \infty$ as

$$\phi_{c,\text{hd}} = \tan^{-1} \left[\frac{f_v^2 - (\Lambda + f_h)f_h - \sqrt{[f_v^2 + (\Lambda + f_h)^2](f_v^2 + f_h^2)}}{f_v(\Lambda + 2f_h)} \right], \quad (120)$$

$$\max(\sigma_{\text{hd}}^{(0)}) = \sqrt{\frac{-f_v^2 - f_h(\Lambda + f_h) + \sqrt{[f_v^2 + (\Lambda + f_h)^2](f_v^2 + f_h^2)}}{2}}. \quad (121)$$

This maximum growth rate is also equivalent to the maximum growth rate (81) of the inertial instability obtained by the WKBJ analysis in the high-diffusivity limit $\kappa_0 \rightarrow \infty$.

Figure 13 shows contours of the growth rate σ in the wavenumber space (k_y, k_z) calculated from the cubic equation (107) for various Re and Pe at $\Omega_0/S_0 = 1$, $\theta = 45^\circ$ and $Ri = 0.1$. For these parameters, σ is positive in the second and fourth quadrants. For the inviscid and non-diffusive case shown in panel a, we see that the growth rate remains constant at a fixed phase angle $\phi = \tan^{-1}(k_z/k_y)$ and reaches its maximum at the critical phase angle $\phi_{c,\text{ld}}$. For a highly-diffusive case at $Pe = 0.01$ shown in panel b, we see that σ is positive in a narrower range of ϕ in the second and fourth quadrants and it remains constant at a fixed phase angle ϕ only for a sufficiently large k . For a small $k \ll 1$, it is unstable in leaf-shaped regions in the second/fourth quadrants. For a viscous case in panel c, the symmetric instability is suppressed and the growth rate is only positive for finite wavenumbers k_y and k_z , which implies that the growth rate now depends on the wavenumber amplitude k . For a fixed k , we verified that the maximum growth rate for viscous cases still occurs at the critical phase angle ϕ_c , which is close to the one $\phi_{c,\text{hd}}$ obtained for the inviscid case in the high-diffusivity limit $\kappa_0 \rightarrow \infty$.

We verified above that the maximum growth rates of the symmetric instability are equal to those of the inertial instability for both low and high-diffusivity limits, if we consider the same shear $\Lambda = S_0$. A question to raise is whether we can compare not only the maximum growth rates of the two instabilities but also their growth rates at arbitrary wavenumbers k_y and k_z . The problem in the inertial instability of the hyperbolic tangent shear flow is that the velocity varies along the z -direction so the vertical wavenumber k_z of inertial instability modes also changes locally as verified in the WKBJ solutions (45) and (67). For instance, for the inviscid and non-diffusive case ($\nu_0 = \kappa_0 = 0$), we can find the following local vertical wavenumber $k_z(z)$ by taking the derivative with respect to z in the exponent of the WKBJ solution (45):

$$k_z(z) = -\frac{k_y f_v (U'(z) + f_h)}{\sigma^2 + f_v^2} \pm k_y \sqrt{-\Delta(z)}, \quad (122)$$

where \pm signs appear due to the two wavelike solutions with non-zero amplitudes B_\pm in the WKBJ solution (45). As we equate the shear Λ of the symmetric instability with the inertial instability shear S_0 evaluated at $z = 0$, we also consider the local wavenumber at $z = 0$ as

$$k_{z,0} \equiv k_z(0) = -\frac{k_y f_v (S_0 + f_h)}{\sigma^2 + f_v^2} \pm k_y \sqrt{-\Delta(0)}, \quad (123)$$

where

$$\Delta(0) = \frac{\sigma^2 + N^2 + f_h(S_0 + f_h)}{\sigma^2 + f_v^2} - \frac{f_v^2 (S_0 + f_h)^2}{(\sigma^2 + f_v^2)^2}. \quad (124)$$

We can formulate the expression (123) as

$$\left[\frac{k_{z,0}}{k_y} + \frac{f_v(S_0 + f_h)}{\sigma^2 + f_v^2} \right]^2 = \left[\frac{f_v^2 (S_0 + f_h)^2}{(\sigma^2 + f_v^2)^2} - \frac{\sigma^2 + N^2 + f_h(S_0 + f_h)}{\sigma^2 + f_v^2} \right], \quad (125)$$

and simplify it as

$$k_{z,0}^2 + 2\frac{k_{z,0}k_y f_v (S_0 + f_h)}{\sigma^2 + f_v^2} + k_y^2 \frac{\sigma^2 + N^2 + f_h(S_0 + f_h)}{\sigma^2 + f_v^2} = 0. \quad (126)$$

This leads to the following growth rate

$$\sigma = \sqrt{\frac{-k_y(k_{z,0}f_v S_0 + k_y N^2) - (k_y f_h + k_{z,0}f_v)[k_{z,0}f_v + k_y(S_0 + f_h)]}{k_{z,0}^2 + k_y^2}}. \quad (127)$$

We see that this growth rate (127) is equal to that of the symmetric instability (110) when $S_0 = \Lambda$.

Similarly, for the high-diffusivity case $\kappa \rightarrow \infty$, we find the following local wavenumber $k_z(z)$ from the WKBJ solution (67):

$$k_z(z) = -\frac{k_y f_v (U' + 2f_h)}{2(\sigma^2 + f_v^2)} \pm k_y \sqrt{-\Gamma(z)}. \quad (128)$$

By taking the local wavenumber at $z = 0$, we find a relation

$$\left[k_{z,0} + \frac{k_y f_v (S_0 + 2f_h)}{2(\sigma^2 + f_v^2)} \right]^2 = k_y^2 \left[\frac{f_v^2 (S_0 + 2f_h)^2}{4(\sigma^2 + f_v^2)^2} - \frac{\sigma^2 + f_h(S_0 + f_h)}{\sigma^2 + f_v^2} \right], \quad (129)$$

which leads to the following growth rate:

$$\sigma = \sqrt{\frac{-(k_y f_h + k_{z,0}f_v)[k_{z,0}f_v + k_y(S_0 + f_h)]}{k_{z,0}^2 + k_y^2}}, \quad (130)$$

which is the same as the growth rate of the symmetric instability (113) when $S_0 = \Lambda$.

As shown by the analysis above, symmetric instability of a linear shear flow $U = \Lambda z$ is closely linked to the inertial instability of a hyperbolic-tangent shear flow. This is an important mathematical result on the inertial instability that shows that the growth rate does not depend on the profile of the shear but it rather depends only on the strength of the shear. We note that this argument is not applicable to the inflectional instability which arises due to an inflection point, a unique feature that depends strongly on the profile of the shear flow. Nevertheless, an advantage of using the symmetric instability is that we have analytic expressions of the growth rate even for finite viscosity ν and diffusivity κ . This is practical when we use the analytical expressions of the growth rate to deduce turbulent viscosity

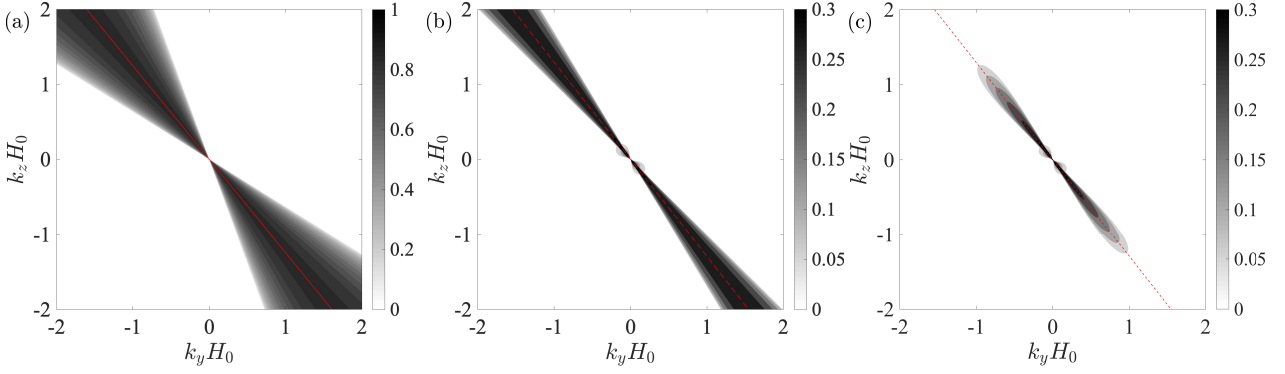


Figure 13. Contours of the growth rate σ/S_0 in the parameter space of wavenumbers (k_y, k_z) for symmetric instability at $\Omega_0/S_0 = 1$, $\theta = 45^\circ$, and $Ri = 0.1$ for (a) $Re = Pe = \infty$, (b) $Re = \infty$ and $Pe = 0.01$, and (c) $Re = 10$ and $Pe = 0.01$. Red solid line in (a) indicates the wavenumber ratio (118) and red dashed lines in (b,c) indicate (120).

models to be implemented in stellar evolution simulations. In the next section, we demonstrate how our results on vertical shear instabilities can further be used to deduce the turbulent effective viscosities and describe turbulent dissipation in stellar radiation zones.

6 TURBULENT TRANSPORT INDUCED BY VERTICAL SHEAR INSTABILITIES

6.1 Evolution of perturbation energy and turbulent effective viscosities

Stability results such as the growth rate, eigenfunction or wavenumbers have been used to construct turbulent viscosity models, which can be derived analytically from a simple eddy viscosity argument with basic scaling laws (Spruit 2002; Fuller et al. 2019; Park et al. 2020, 2021). Numerical simulations of turbulence in a shearing box can also be used to formulate and compute turbulent effective viscosities. For instance, nonlinear simulations of the GSF instability using a local Cartesian model at either the equator (Barker et al. 2019) or at a general latitude (Barker et al. 2020; Dymott et al. 2023) can provide the characteristics of turbulence driven by the GSF instability. From these turbulence simulations, an effective viscosity ν_E is suggested to follow a scaling as $\nu_E = \nu_0 \Omega_0^2 S_0^{-1} N^{-1} Pr^{-1/2} < u_x u_y >$ where we use here our notations such as S_0 or Ω_0 to facilitate the comparison and $< u_x u_y >$ is the averaged Reynolds stress of the order $O(10) - (100)$ obtained from their simulations.

In this section, we will use linear stability analysis results to examine turbulent dissipation induced by vertical shear instabilities and deduce turbulent viscosity models. The proposed viscosity models are similar to those from previous studies but we will derive them by considering more specifically nonlinear saturation of shear instabilities based on the perturbation energy argument. We will focus on how turbulent dissipation depends on the two different instabilities (i.e. the inertial and inflectional ones) and parameters such as the Péclet number Pe , the Prandtl number Pr or the Richardson number Ri . To do so, we first define the total energy of perturbation per unit density as

$$\tilde{E} = \frac{1}{2} \langle \tilde{u}^2 + \tilde{v}^2 + \tilde{w}^2 + N^2 \tilde{\mathcal{T}}^2 \rangle, \quad (131)$$

(see also, Park et al. 2017) where $\tilde{\mathcal{T}} = \tilde{T}/\mathcal{T}_\Theta$ is the normalized temperature and $< \cdot >$ denotes the volume integral defined as

$$\langle \tilde{X} \rangle = \int_{-l_x}^{l_x} \int_{-l_y}^{l_y} \int_{-l_z}^{l_z} \tilde{X} dx dy dz, \quad (132)$$

where (l_x, l_y, l_z) are the domain lengths in the Cartesian coordinate defined as $l_x = \pi/k_x$, $l_y = \pi/k_y$, $l_z = \pi/k_z$ or $l_z \rightarrow \infty$ if the boundary conditions are non-periodic and open in the z -direction. The total energy per unit density \tilde{E} is comprised of the kinetic energy per unit density \tilde{E}_K and potential energy per unit density \tilde{E}_P as $\tilde{E} = \tilde{E}_K + \tilde{E}_P$ where

$$\tilde{E}_K = \frac{1}{2} \langle \tilde{u}^2 + \tilde{v}^2 + \tilde{w}^2 \rangle, \quad \tilde{E}_P = \frac{1}{2} \langle N^2 \tilde{\mathcal{T}}^2 \rangle. \quad (133)$$

After some manipulations applied to the perturbation equations (10)-(13), we can express the time evolution of the total perturbation energy as

$$\begin{aligned} \frac{\partial \tilde{E}}{\partial t} = & - \langle U' \tilde{u} \tilde{w} \rangle + \langle U' f_v \tilde{v} \tilde{\mathcal{T}} \rangle - \nu_0 \left(\left(\frac{\partial \tilde{u}}{\partial x} \right)^2 + \left(\frac{\partial \tilde{u}}{\partial y} \right)^2 + \left(\frac{\partial \tilde{u}}{\partial z} \right)^2 \right. \\ & + \left(\frac{\partial \tilde{v}}{\partial x} \right)^2 + \left(\frac{\partial \tilde{v}}{\partial y} \right)^2 + \left(\frac{\partial \tilde{v}}{\partial z} \right)^2 + \left(\frac{\partial \tilde{w}}{\partial x} \right)^2 + \left(\frac{\partial \tilde{w}}{\partial y} \right)^2 + \left. \left(\frac{\partial \tilde{w}}{\partial z} \right)^2 \right) \\ & - N^2 \kappa_0 \left(\left(\frac{\partial \tilde{\mathcal{T}}}{\partial x} \right)^2 + \left(\frac{\partial \tilde{\mathcal{T}}}{\partial y} \right)^2 + \left(\frac{\partial \tilde{\mathcal{T}}}{\partial z} \right)^2 \right). \end{aligned} \quad (134)$$

We note that there is no contribution from pressure and nonlinear terms after the continuity equation (9) is taken into account (see also, Schmid & Henningson 2001). The viscous and thermal dissipations act a stabilizing role on the perturbation energy with positive ν_0 and κ_0 while the shear U' can either destabilize or stabilize depending on the signs of \tilde{u} , \tilde{w} , \tilde{v} and $\tilde{\mathcal{T}}$. The first term on the right-hand side of (134) represents the growth by the Orr mechanism when the shear U' is negatively correlated with $\tilde{u} \tilde{w}$ (Orr 1907). The second term denotes the energy growth occurring when the vertical Coriolis parameter f_v is non-zero and positive (negative) and the shear U' is positively (negatively) correlated with $\tilde{v} \tilde{\mathcal{T}}$. If we apply the normal mode (18) to the equation (134), we obtain the following equation

$$\begin{aligned} 2\sigma_r \hat{E} = & \int_{-l_z}^{l_z} U' \left[\frac{f_v (\hat{v} \hat{\mathcal{T}}^* + \hat{v}^* \hat{\mathcal{T}}) - (\hat{u} \hat{w}^* + \hat{u}^* \hat{w})}{2} \right] dz \\ & - \nu_0 \int_{-l_z}^{l_z} \left[k^2 (|\hat{u}|^2 + |\hat{v}|^2 + |\hat{w}|^2) + \left| \frac{\partial \hat{u}}{\partial z} \right|^2 + \left| \frac{\partial \hat{v}}{\partial z} \right|^2 + \left| \frac{\partial \hat{w}}{\partial z} \right|^2 \right] dz \\ & - N^2 \kappa_0 \int_{-l_z}^{l_z} \left[k^2 |\hat{\mathcal{T}}|^2 + \left| \frac{\partial \hat{\mathcal{T}}}{\partial z} \right|^2 \right] dz, \end{aligned} \quad (135)$$

where \hat{E} is the modal energy per unit density defined as

$$\hat{E} = \int_{-l_z}^{l_z} \left(|\hat{u}|^2 + |\hat{v}|^2 + |\hat{w}|^2 + N^2 |\hat{T}|^2 \right) dz. \quad (136)$$

Let us now consider a nonlinear saturation process where perturbations grow due to vertical shear instabilities and reach an equilibrium state. At this nonlinearly-saturated equilibrium state, there is no growth (i.e., $\sigma_r = 0$) and the base flow is distorted as $U + \delta U$, balancing with the modified perturbations $\hat{\mathbf{q}} + \delta \hat{\mathbf{q}}$ where $\hat{\mathbf{q}} = (\hat{u}, \hat{v}, \hat{w}, \hat{T})$. These base and perturbation states at nonlinear saturation with $\sigma_r = 0$ lead to the following equation:

$$\begin{aligned} 0 &= \int_{-l_z}^{l_z} (U' + \delta U') \left[\frac{f_v (\hat{v} \hat{T}^* + \hat{v}^* \hat{T}) - (\hat{u} \hat{w}^* + \hat{u}^* \hat{w})}{2} \right] dz \\ &- \nu_0 \int_{-l_z}^{l_z} \left[k^2 (|\hat{u}|^2 + |\hat{v}|^2 + |\hat{w}|^2) + \left| \frac{\partial \hat{u}}{\partial z} \right|^2 + \left| \frac{\partial \hat{v}}{\partial z} \right|^2 + \left| \frac{\partial \hat{w}}{\partial z} \right|^2 \right] dz \\ &- N^2 \kappa_0 \int_{-l_z}^{l_z} \left[k^2 |\hat{T}|^2 + \left| \frac{\partial \hat{T}}{\partial z} \right|^2 \right] dz + O(\delta \hat{\mathbf{q}}), \end{aligned} \quad (137)$$

where $O(\delta \hat{\mathbf{q}})$ denotes the term of order δ due to the distortion in perturbation mode shape $\delta \hat{\mathbf{q}}$. In the process of nonlinear saturation, both distortions δU and $\delta \hat{\mathbf{q}}$ are important and they interact each other to generate turbulent transport. However, if we assume that the changes in perturbation is negligible (i.e. $\delta \hat{\mathbf{q}} = 0$; see also, [Stuart 1958](#)) and if we introduce a turbulent effective viscosity ν_v that presumably maintains the balance between the base flow distortion and turbulent dissipation as follows:

$$\begin{aligned} \delta U' \left[\frac{f_v (\hat{v} \hat{T}^* + \hat{v}^* \hat{T}) - (\hat{u} \hat{w}^* + \hat{u}^* \hat{w})}{2} \right] &= \\ -\nu_v \int_{-l_z}^{l_z} \left[k^2 (|\hat{u}|^2 + |\hat{v}|^2 + |\hat{w}|^2 + N^2 |\hat{T}|^2) \right. & \\ \left. + \left| \frac{\partial \hat{u}}{\partial z} \right|^2 + \left| \frac{\partial \hat{v}}{\partial z} \right|^2 + \left| \frac{\partial \hat{w}}{\partial z} \right|^2 + N^2 \left| \frac{\partial \hat{T}}{\partial z} \right|^2 \right] & \end{aligned} \quad (138)$$

which implies the turbulent energy growth induced by the shear distortion $\delta U'$ balances with turbulent dissipation with ν_v as a turbulent viscosity coefficient, we can find the following relation for ν_v in terms of the energy \hat{E} and the growth rate σ_r :

$$\begin{aligned} \nu_v \int_{-l_z}^{l_z} \left[k^2 (|\hat{u}|^2 + |\hat{v}|^2 + |\hat{w}|^2 + N^2 |\hat{T}|^2) + \left| \frac{\partial \hat{u}}{\partial z} \right|^2 + \left| \frac{\partial \hat{v}}{\partial z} \right|^2 \right. & \\ \left. + \left| \frac{\partial \hat{w}}{\partial z} \right|^2 + N^2 \left| \frac{\partial \hat{T}}{\partial z} \right|^2 \right] dz &= 2\sigma_r \hat{E}. \end{aligned} \quad (139)$$

Although the neglect of the perturbation distortion $\delta \hat{\mathbf{q}}$ may not reflect precise turbulent processes, the equation (139) is still crucial as it shows a clear link between the turbulent effective viscosity and the growth rate of the vertical shear instabilities. If $k_x = 0$ is considered like in the case of symmetric instability, we obtain the following simplified equation

$$\nu_v (k_y^2 + k_z^2) 2\hat{E} = 2\sigma_r \check{E}, \quad (140)$$

where $\check{E} = |\hat{u}|^2 + |\hat{v}|^2 + |\hat{w}|^2 + N^2 |\hat{T}|^2$. This implies

$$\nu_v = \frac{\sigma_r}{k_y^2 + k_z^2}. \quad (141)$$

The turbulent viscosity ν_v expressed in terms of the growth rate σ_r is

equivalent to the one proposed by [Spruit \(2002\)](#); [Fuller et al. \(2019\)](#) where the turbulent viscosity is proportional to the growth rate. We note that, while they propose the turbulent viscosity based on a simple scaling law, our model (141) is derived using the perturbation energy argument and nonlinear saturation of the instability.

6.2 Turbulent viscosities for inertial and inflectional instabilities

From the above analysis, we propose a general turbulent viscosity model using the growth rate and wavenumbers as

$$\nu_v = \frac{\sigma}{k^2}, \quad (142)$$

where $k^2 = k_x^2 + k_y^2 + k_z^2$. Due to the inhomogeneity in the vertical z -direction for the hyperbolic tangent shear flow (5), it is not straightforward to quantify the wavenumber k_z . For the inflectional instability that has the maximum growth rate in the range $|k_x H_0| < 1$ at $|k_y| = |k_{y,\min}|$, we can approximate $k_z H_0 \approx 1$ based on the observation that eigenfunctions are localised around the sheared region (see e.g. [Fig. 3a](#)). The situation is more complicated with the inertial instability that has the maximum growth rate for large k_y at $k_x = 0$. On the one hand, for small $|k_y H_0| < 1$, we expect a similar scaling law as $k_z H_0 \approx 1$. On the other hand, for large $|k_y H_0| > 1$, the eigenfunction is localised around the centre $z = 0$ and has a small vertical length scale as $1/|k_y|$ (i.e. $|k_z| \approx |k_y|$), which can also be presumed from the quantization conditions such as [Eq. \(58\)](#). Therefore, for the inertial instability, we assume $k_z H_0 = \max(1, k_y H_0)$.

Panel a of [Fig. 14](#) shows examples of the turbulent viscosity ν_v versus k^2 for the inertial instability at $Pe = 0.01$, $Pr = 10^{-6}$, $Ri = 0.25$ and $\Omega_0/N = 0.2$ for different latitudes $\theta = 0, 30, 60^\circ$. The growth rate of the inertial instability becomes zero at $k_y = 0$, thus the viscosity ν_v becomes zero at $k^2 H_0^2 = 1$ (i.e. $k_x = k_y = 0$, $k_z H_0$ is considered to be 1). ν_v increases sharply as k^2 increases from the unity and reaches its peak before it decays exponentially. It is not shown here but this feature is similarly observed for ν_v of the inflectional instability computed at $|k_y| = |k_{y,\min}|$ while varying k_x . By picking up the maximum ν_v over the range of k^2 at a given ratio Ω_0/N and a colatitude θ , we compute contours of the maximum viscosity $\nu_{v,\max}$ for the inertial and inflectional instabilities at $Pe = 0.01$, $Pr = 10^{-6}$ and $Ri = 0.25$ as shown in [Fig. 14](#) panels b and c. For the inertial case in panel b, we see that $\nu_{v,\max}$ is maximal at the poles $\theta = 0, 180^\circ$ around $\Omega_0/N = 0.2$. As it is inertially stable near the equator, we see that $\nu_{v,\max}$ is zero around the equator. The inertial instability is driven by the rotation Ω_0 , thus $\nu_{v,\max}$ is also zero at $\Omega_0/N = 0$. This parametric dependence of $\nu_{v,\max}$ in the parameter space $(\Omega_0/N, \theta)$ is different that of the inflectional instability as shown in panel c. Without rotation (i.e. $\Omega_0 = 0$), the inflectional instability is independent of the colatitude θ so as the viscosity $\nu_{v,\max}$. As Ω_0/N increases, $\nu_{v,\max}$ is maximal at the equator and decreases as the latitude is away from the equator, the feature similar to the growth rate contours in [Fig. 4c](#). Same as the growth rate, the viscosity ν_v is constant and independent of the ratio Ω_0/N at the equator. We also found that, at a certain colatitude θ_c (namely the cut-off colatitude hereafter), the growth rate of the inflectional instability decreases sharply and becomes smaller than the growth rate of the inertial instability whose maximum is attained at $k_x = 0$ and $|k_y| = |k_{y,\min}|$. This happens for $\Omega_0/N > 0.12$, the regime in which the inertial instability co-exists and dominates the inflectional instability. In panel c, we distinguish the turbulent dissipation induced by the inflectional instability from that by the inertial instability by filtering the viscosity outside the cut-off

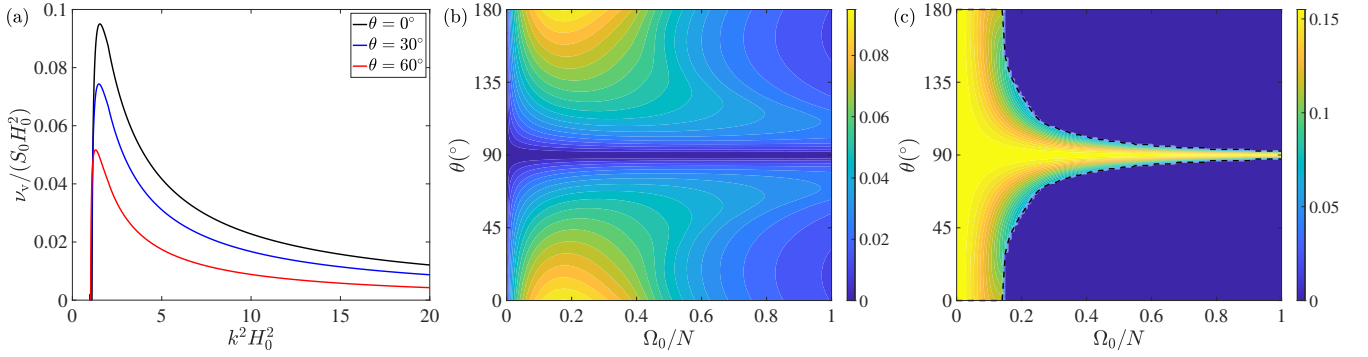


Figure 14. (a) Turbulent viscosity ν_v for the inertial instability computed at $Pe = 0.01$, $Pr = 10^{-6}$, $Ri = 0.25$ and $\Omega_0/N = 0.2$ for different colatitudes θ . (b,c) Contours of the maximum turbulent viscosity $\nu_{v,\max}$ at $Pe = 0.01$, $Pr = 10^{-6}$ and $Ri = 0.25$ for (b) the inertial instability and (c) the inflectional instability. The black dashed line in panel c denotes the cut-off colatitude θ_c at which the inertial instability dominates the inflectional instability.

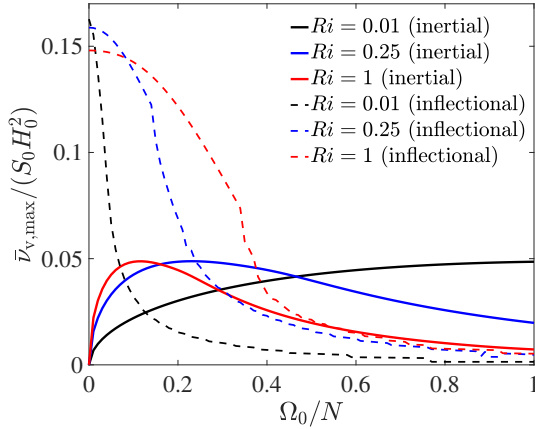


Figure 15. Latitudinally-averaged turbulent viscosity $\bar{\nu}_{v,\max}$ versus the ratio Ω_0/N for the inertial (solid lines) and inflectional (dashed lines) instabilities for $Ri = 0.01$ (black), $Ri = 0.25$ (blue) and $Ri = 1$ (red) at $Pe = 0.01$ and $Pr = 10^{-6}$.

colatitude θ_c . For the same parameters $Pe = 0.01$, $Pr = 10^{-6}$ and $Ri = 0.25$ considered here, we see in panels b and c that the maximum of $\nu_{v,\max}$ for the inflectional instability is higher while contours of $\nu_{v,\max}$ for the inertial instability span wider in the parameter space $(\Omega_0/N, \theta)$. From these contours in panels b and c, we see that the turbulent dissipation induced by the inertial instability is strong near the poles while the dissipation induced by the inflectional instability is strong near the equator.

In Fig. 15, we plot the latitudinally-averaged turbulent viscosity $\bar{\nu}_{v,\max}(\Omega_0/N)$ defined as

$$\bar{\nu}_{v,\max} = \frac{1}{2} \int_0^\pi \nu_{v,\max}(\Omega_0/N, \theta) \sin \theta d\theta, \quad (143)$$

for different values of Ri at $Pe = 0.01$ and $Pr = 10^{-6}$. For the inflectional instability, we see that the viscosity $\bar{\nu}_{v,\max}$ is maximal for the non-rotating case $\Omega_0 = 0$ and decreases as the ratio Ω_0/N increases. While the $\bar{\nu}_{v,\max}$ curves descend as Ri increases when Ω_0/N is close to zero, as predicted by Zahn (1992) in which the Coriolis acceleration is neglected (i.e. $\Omega_0/N = 0$), the viscosity $\bar{\nu}_{v,\max}$ increases and the overall curves ascend with increasing Ri when Ω_0/N is large. We found that the turbulent viscosity for the inflectional instability is large and positive only for strong thermal diffusion with low Pe as $Pe \ll 1$. For weak thermal diffusion with

$Pe \geq 1$, the growth rate σ decays sharply as the latitude is away from the equator and thus the averaged viscosity $\bar{\nu}_{v,\max}$ becomes zero.

For the inertial instability, $\bar{\nu}_{v,\max}$ is zero at $\Omega_0/N = 0$ and increases as Ω_0/N increases. After the viscosity reaches its peak, it decays monotonically with the ratio Ω_0/N . For the same $Pe = 0.01$ and $Pr = 10^{-6}$, the averaged turbulent viscosity $\bar{\nu}_{v,\max}$ of the inertial instability becomes larger than that of the inflectional instability for large Ω_0/N . It is also shown that, as the stratification increases (i.e. Ri increases), the curves for the averaged turbulent viscosity $\bar{\nu}_{v,\max}$ shrink with their peaks moving towards $\Omega_0/N = 0$. The trend with varying Ri is opposite for the inflectional instability as the overall curves move away from $\Omega_0/N = 0$ as Ri increases. This implies that the inflectional instability plays an important role in turbulent transport for strongly-stratified slowly-rotating stars (i.e. high Ri and low Ω_0/N) while the inertial instability becomes more important for weakly-stratified fast-rotating stars (i.e. low Ri and high Ω_0/N).

Our proposition of a new turbulent viscosity model such as (142) or the latitudinally-averaged one (143) advances our understanding of turbulent transport (and mixing) in stellar radiation zones as the model (i) includes the effect of the full Coriolis acceleration to account for turbulent dissipation at a general latitude and (ii) distinguishes the contribution to turbulence induced by the inflectional instability from that by the inertial instability.

Our model is, however, deduced from a linear framework and is required to be compared and validated against results from nonlinear numerical simulations. Further analytical and numerical investigations are, therefore, crucial and should be conducted to propose a more complete modelling of turbulence to be implemented in 1-D and 2-D stellar structure and evolution codes, as previously studied in Mathis et al. (2018) in the case of 1-D codes.

7 CONCLUSION

In this paper, we study vertical shear instabilities induced by differential rotation along the radial direction in stellar radiation zones where fluid is stably stratified and the seat of a strong thermal diffusion. The novelty in this study is that we consider the effects of thermal diffusion and the full Coriolis acceleration, the latter considering both the vertical and horizontal rotation components, on vertical shear instabilities. This configuration allows us to explore shear instabilities at any latitude where the rotation vector is not perpendicular but is inclined to the local plane of stellar radiation zones where the thermal diffusion is strong. To explore

[!t]

Table 1. Summary table for vertical shear instabilities and their variation with the full Coriolis acceleration and thermal diffusion

Instability type	$\kappa_0 \uparrow$ ($Pe \downarrow$)	$\Omega_0/N \uparrow$	Maximum turbulent transport at high κ_0
Inflectional	\uparrow	\downarrow (except at $\theta = 90^\circ$)	Near the equator ($\theta = 90^\circ$)
Inertial	\uparrow	\uparrow (small Ω_0/N) \downarrow (large Ω_0/N)	Near the poles ($\theta = 0^\circ, 180^\circ$)

vertical shear instabilities, we consider a canonical shear flow with a hyperbolic-tangent profile and analyse its stability in stably stratified, thermally-diffusive, and rotating fluids with the full Coriolis acceleration. Two types of instabilities are identified: the inflectional instability due to an inflection point of the shear flow and the inertial instability occurring due to an imbalance between the centrifugal acceleration and pressure gradient. The inflectional instability is found to be destabilized as either thermal diffusion becomes stronger or stratification becomes weaker. The regime of inflectional instability exists in a narrow wavenumber range $k_x < 1$ and the instability is maximal at $k_y = 0$ or $k_y = k_{y,\min}$ if the wide-jet approximation is considered for cases outside the equator. At the equator with $f_v = 0$, the maximum growth rate of the inflectional instability is independent of the horizontal rotation component f_h . At a general latitude with non-zero f_v , the inflectional instability is suppressed as the ratio Ω_0/N increases at a co-latitude θ outside the equator. While parametric dependence of the inertial instability on stratification and thermal diffusion is similar to that of the inflectional instability, the effect of the full Coriolis acceleration on the inertial instability is different. In non-diffusive fluids, the inertial instability is found to be maximal in the mid latitudes for the cyclonic rotation with $\Omega_0/S_0 > 0$. For highly-diffusive fluids, a case more relevant to stellar radiation zones, the inertial instability and its turbulent dissipation are maximal at the poles. These findings are confirmed by both numerical linear stability analysis and the WKBJ analysis with explicit expressions of the dispersion relation for inertial instability. Furthermore, it is revealed that symmetric instability, which is analytically more approachable as a linear shear flow is considered in the analysis, is found to be analogous not only qualitatively but also quantitatively to the inertial instability of a hyperbolic-tangent shear flow when the same value of the vertical shear at $z = 0$ is considered for both cases. As a consequence of these results, we foresee that the inflectional instability plays a key role for turbulent transport and mixing in the equatorial region of strongly-stratified radiation zones of slowly-rotating stars while the inertial instability will promote turbulent transport in the polar regions of weakly-stratified radiation zones in fast-rotating stars. The summary of our findings on vertical shear instabilities is provided in Table 1.

In this work, we have thus provided a first complete linear analysis of vertical shear instabilities with taking simultaneously the full Coriolis acceleration and potentially strong heat diffusion into account. The prescriptions we have computed for the vertical eddy viscosity to model the turbulent transport of momentum and chemicals are ready to be implemented in 2D stellar structure and evolution numerical models. They can also be implemented in 1D models by making an average over latitudes. The next steps will be to undertake the non-linear study of the inflectional and inertial instabilities of a vertical shear using direct numerical simulations, to study the instabilities of shear varying both with the radius and the co-latitude (e.g. [Garau et al. 2024](#)), and to evaluate the effects of the presence of a potential magnetic field (e.g. [Lecoanet et al. 2010](#)) by taking the full Coriolis

acceleration and heat diffusion into account. This would contribute to build step by step a complete picture of shear instabilities in stellar radiation zones, which can be used in forthcoming generations of stellar structure and evolution models.

ACKNOWLEDGEMENTS

J. Park acknowledges support from the Royal Astronomical Society and Office of Astronomy for Development through the RAS-OAD astro4dev grant and from the Engineering and Physical Sciences Research Council (EPSRC) through the EPSRC mathematical sciences small grant (EP/W019558/1). The authors acknowledge support from the European Research Council through ERC grant SPIRE 647383. S. Mathis acknowledges support from the European Research Council (ERC) under the Horizon Europe programme (Synergy Grant agreement 101071505: 4D-STAR), from the CNES SOHO-GOLF and PLATO grants at CEA-DAp, and from PNPS (CNRS/INSU). While partially funded by the European Union, views and opinions expressed are however those of the author only and do not necessarily reflect those of the European Union or the European Research Council. Neither the European Union nor the granting authority can be held responsible for them.

DATA AVAILABILITY

The data underlying this article will be shared on reasonable request to the corresponding author.

REFERENCES

- Abramowitz M., Stegun I. A., 1972, *Handbook of Mathematical Functions with Formulas, Graphs, and Mathematical Tables*. Dover Publications
- Antkowiak A., 2005, PhD thesis, Université Paul Sabatier de Toulouse
- Arobone E., Sarkar S., 2012, *J. Fluid Mech.*, 703, 29
- Barker A., Jones C. A., Tobias S. M., 2019, *MNRAS*, 487, 1777
- Barker A., Jones C. A., Tobias S. M., 2020, *MNRAS*, 495, 1468
- Billant P., Gallaire F., 2005, *J. Fluid Mech.*, 542, 365
- Billant P., Le Dizès S., 2009, *Phys. Fluids*, 21, 106602
- Brüggen M., Hillebrandt W., 2001, *MNRAS*, 320, 73
- Cantiello M., Mankovich C., Bildsten L., Christensen-Dalsgaard J., Paxton B., 2014, *ApJ*, 788, 93
- Caulfield C. P., 2021, *Annu. Rev. Fluid Mech.*, 53, 113
- Chaboyer B., Zahn J.-P., 1992, *A&A*, 253, 173
- Chang E., Garaud P., 2021, *MNRAS*, 506, 4914
- Decressin T., Mathis S., Palacios A., Siess L., Talon S., Charbonnel C., Zahn J. P., 2009, *A&A*, 495, 271
- Deheuvels S., et al., 2014, *A&A*, 564, A27
- Deloncle A., Chomaz J.-M., Billant P., 2007, *J. Fluid Mech.*, 570, 297–305
- Dhouib H., Prat V., Van Reeth T., Mathis S., 2021, *A&A*, 652, A154
- Dintrans B., Rieutord M., 2000, *A&A*, 354, 86
- Drazin P. G., 2015, *Encyclopedia of Atmospheric Sciences*, pp 343–346kno
- Dymott R. W., Barker A. J., Jones C. A., Tobias S. M., 2023, *MNRAS*, 524, 2857

- Eaves T. S., Balmforth N. J., 2019, *J. Fluid Mech.*, 860, 145
- Espinosa Lara F., Rieutord M., 2013, *A&A*, 552, A35
- Fabre D., Jacquin L., 2004, *J. Fluid Mech.*, 500, 239
- Fricke K., 1968, *Z. Astrophys.*, 68, 317
- Fuller J., Piro A. L., Jermyn A. S., 2019, *MNRAS*, 485, 3661
- Gallet F., Bouvier J., 2015, *A&A*, 577, A98
- Garaud P., 2002, *MNRAS*, 335, 707
- Garaud P., 2021, *Phys. Rev. Fluids*, 6, 030501
- Garaud P., Khan S., Brown J. M., 2024, *ApJ*, 961, 220
- Goldreich P., Schubert G., 1967, *ApJ*, 150, 571
- Heger A., Langer N., Woosley S. E., 2000, *ApJ*, 528, 368
- Heger A., Woosley S. E., Spruit H. C., 2005, *ApJ*, 626, 350
- Helmholtz H., 1868, *Phil. Mag.*, 36, 337
- Holmboe J., 1962, *Geofys. Publ.*, 24, 67
- Holton J., 2004, *An Introduction to Dynamic Meteorology*. Elsevier Academic Press
- Jouve L., Lignières F., Gaurat M., 2020, *A&A*, 641, A13
- Kelvin L., 1871, *Phil. Mag.*, 42, 362
- Klaassen G. P., Peltier W. R., 1985, *J. Fluid Mech.*, 155, 1
- Kloosterziel R. C., van Heijst G. J. F., 1991, *J. Fluid Mech.*, 223, 1
- Kulenthirarajah L., Garaud P., 2018, *ApJ*, 864, 107
- Le Dizès S., Lacaze L., 2005, *J. Fluid Mech.*, 542, 69
- Lecoanet D., Zweibel E. G., Townsend R. H. D., Huang Y.-M., 2010, *ApJ*, 712, 1116
- Lee U., Saio H., 1997, *ApJ*, 491, 839
- Lignières F., Califano F., Mangeney A., 1999, *A&A*, 349, 1027
- Maeder A., 1995, *A&A*, 299, 84
- Maeder A., 2009, *Physics, Formation and Evolution of Rotating Stars*. Springer Berlin Heidelberg
- Maeder A., Meynet G., 1996, *A&A*, 313, 140
- Maeder A., Meynet G., 2004, *A&A*, 422, 225
- Marques J. P., et al., 2013, *A&A*, 549, A74
- Mathis S., 2009, *A&A*, 506, 811
- Mathis S., Prat V., 2019, *A&A*, 631, A26
- Mathis S., Prat V., Amard L., Charbonnel C., Palacios A., Lagarde N., Eggenberger P., 2018, *A&A*, 620, A22
- Meynet G., Maeder A., 2000, *A&A*, 361, 101
- Miles J. W., 1961, *J. Fluid Mech.*, 10, 496
- Mirouh G. M., Baruteau C., Rieutord M., Ballot J., 2016, *Journal of Fluid Mechanics*, 800, 213
- Mombarg J. S. G., Rieutord M., Espinosa Lara F., 2023, *A&A*, 677, L5
- Mombarg J. S. G., Rieutord M., Espinosa Lara F., 2024, *A&A*, 683, A94
- Mosser B., et al., 2012, *A&A*, 548, A10
- Olver F. W. J., 1974, *Asymptotics and Special Functions*. Academic Press, New York
- Orr W. M. F., 1907, *Proc. R. Irish Acad. A*, 27, 69
- Ortiz S., Chomaz J.-M., T. L., 2002, *Phys. Fluids*, 14, 2585
- Park J., 2012, PhD thesis, Ecole Polytechnique
- Park J., Billant P., 2013a, *Phys. Fluids*, 25, 086601
- Park J., Billant P., 2013b, *J. Fluid Mech.*, 725, 262
- Park J., Billant P., Baik J.-J., 2017, *J. Fluid Mech.*, 822, 80–108
- Park J., Prat V., Mathis S., 2020, *A&A*, 635, A133
- Park J., Prat V., Mathis S., Bugnet L., 2021, *A&A*, 646, A64
- Prat V., Lignières 2013, *A&A*, 551, L3
- Prat V., Lignières F., 2014a, *A&A*, 566, A110
- Prat V., Lignières 2014b, *A&A*, 566, A110
- Rieutord M., 2006, *A&A*, 451, 1025
- Rieutord M., Espinosa Lara F., Putigny B., 2016, *Journal of Computational Physics*, 318, 277
- Royer F., Zorec J., Gómez A. E., 2007, *A&A*, 463, 671
- Schmid P., Henningson D. S., 2001, *Stability and Transition in Shear Flows*. Springer-Verlag, New York
- Spruit H. C., 1999, *A&A*, 349, 189
- Spruit H. C., 2002, *A&A*, 381, 923
- Stuart J. T., 1958, *J. Fluid Mech.*, 4, 1
- Talon S., Charbonnel C., 2005, *A&A*, 440, 981
- Talon S., Zahn J.-P., 1997, *A&A*, 317, 749
- Talon S., Zahn J. P., Maeder A., Meynet G., 1997, *A&A*, 322, 209
- Tort M., Ribstein B., Zeitlin V., 2016, *J. Fluid Mech.*, 788, 274
- Van Reeth T., Tkachenko A., Aerts C., 2016, *A&A*, 593, A120
- Wang P., McWilliams J. C., Ménesguen C., 2014, *J. Fluid Mech.*, 755, 397
- Zahn J.-P., 1983, in Cox A. N., Vauclair S., Zahn J. P., eds, *Saas-Fee Advanced Course 13: Astrophysical Processes in Upper Main Sequence Stars*. p. 253
- Zahn J.-P., 1992, *A&A*, 265, 115
- Zeitlin V., 2018, *Phys. Fluids*, 30, 061701

This paper has been typeset from a $\text{\TeX}/\text{\LaTeX}$ file prepared by the author.